APL Photonics

Thermoplasmonics of metal layers and nanoholes

Cite as: APL Photonics **6**, 101101 (2021); https://doi.org/10.1063/5.0057185
Submitted: 18 May 2021 • Accepted: 29 September 2021 • Accepted Manuscript Online: 30 September 2021 • Published Online: 28 October 2021

Benoit Rogez, Zakaria Marmri, Franck Thibaudau, et al.

Thermoplasmonics of metal layers and nanoholes

Cite as: APL Photon. 6, 101101 (2021); doi: 10.1063/5.0057185
Submitted: 18 May 2021 • Accepted: 29 September 2021 •
Published Online: 28 October 2021

Benoit Rogez,[1,a)] Zakaria Marmri,[2] Franck Thibaudau,[2] and Guillaume Baffou[1,b)]

AFFILIATIONS

[1] Institut Fresnel, CNRS, Aix Marseille Univ, Centrale Marseille, Marseille, France
[2] Aix Marseille Univ, CNRS, CINaM, Marseille, France

[a)] Electronic mail: benoit.rogez@fresnel.fr
[b)] Author to whom correspondence should be addressed: guillaume.baffou@fresnel.fr

ABSTRACT

Since the early 2000s, the experimental and theoretical studies of photothermal effects in plasmonics have been mainly oriented toward systems composed of nanoparticles, mostly motivated by applications in biomedecine, and have overlooked the case of plasmonic resonances of nanoholes in metal layers (also called nanopores or nano-apertures). Yet, more and more applications based on plasmonic nanoholes have been reported these last years (e.g., optical trapping, molecular sensing, and surface-enhanced Raman scattering), and photothermal effects can be unexpectedly high for this kind of systems, mainly because of the very large amount of metal under illumination, compared with nanoparticle systems. Nanoholes in metal layers involve a fully different photothermodynamical picture, and few of what is known about nanoparticles can be applied with nanoholes. A plasmonic nanohole mixes localized and surfaces plasmons, along with heat transport in a two-dimensional highly conductive layer, making the underlying photothermodynamical physics particularly complex. This Tutorial is aimed to provide a comprehensive description of the photothermal effects in plasmonics when metal layers are involved, based on experimental, theoretical, and numerical results. Photothermal effects in metal layers (embedded or suspended) are first described in detail, followed by the study of nanoholes, where we revisit the concept of absorption cross section and discuss the influences of parameters such as layer thickness, layer composition, nanohole size and geometry, adhesion layer, thermal radiation, and illumination wavelength.

I. INTRODUCTION

Metal layers and nanoparticles, embedded in dielectric media, are the two main families of objects widely used in plasmonics. Layers exhibit surface plasmon resonances (SPRs), while nanoparticles undergo localized plasmon resonances (LPRs).[1,2] On the one hand, nanoparticles (typically <100 nm) and their associated LPR have attracted strong interest for applications in bio-medicine,[3] SERS (surface-enhanced Raman scattering),[4] molecular (bio)sensing,[5,6] nanochemistry,[7–9] or solar light harvesting,[8,10–12] among others. On the other hand, plasmonic layers (typically 30–100 nm thick) and their associated SPRs have led to much fewer applications, albeit at the basis of the most accomplished application of plasmonics, that is, SPR biosensing.[13,14] The interest of plasmonic layers can be further enriched when drilled with nanoholes (called also nanopores or nano-apertures), either single or as a periodic array,[15,16] for applications in molecular optical sensing,[17,18] single molecule detection,[19] optical trapping,[19–25] DNA manipulation,[26,27] extraordinary transmission through nanohole arrays,[28,29] photovoltaics,[30] SERS,[31,32] nanochemistry,[33] and thermoplasmonics.[34–36]

In all the plasmonic systems described above, the unavoidable heat generation in the metal due to light absorption is a natural concern. Depending on the application, photothermal effects can be either detrimental (for optical sensing, SERS, etc.) or, on the contrary, the targeted mechanism (cancer therapy,[37] nanochemistry,[38] etc.). When dealing with photothermal effects, the literature on plasmonic *nanoparticles* is now abundant and constitutes the field of thermoplasmonics, born in the early 2000s.[39–42] Many theoretical and experimental studies have been reported on the photothermal effects of nanoparticles of many compositions, under cw or pulsed illumination, over many ranges of wavelengths and powers, and for numerous applications, in particular for bio-medicine, bioimaging, microfluidics, and nanochemistry. In contrast, photothermal effects in metal layers have drawn much less attention. In the mid-2000s, Passian and co-workers used heating of plain plasmonic layers in the Kretschman configuration as a means to

modulate a light beam intensity[43,44] and to study the dynamics of liquid droplets[45] on a plain metal layer. Several studies have also shown that nanoholes can enhance light absorption compared with plain metal layers.[34,35] However, the common belief is that any temperature increase is supposed to be seriously damped by the presence of a metal layer, acting as an efficient heat sink due to its high thermal conductivity.[46] This idea held until very recently when observable temperature increases have been demonstrated in optical trapping experiments with nanoholes illuminated with a focused laser beam.[47] This observation led the authors to revisit the actual mechanisms into play in plasmonic trapping experiments. Today, there is no consensual and comprehensive description of the photothermodynamics of plasmonic layers with or without nanoholes.

This lesser interest in SPR vs LPR photothermal effects is mainly due, we believe, to four reasons. First, for most SPR applications, photothermal effects are not the main process of interest. They are even detrimental. Second, they have been assumed to be insignificant,[46] but this has been questioned recently.[47,48] Third, photothermal effects of metal layers and nanoholes are much more complicated to address, predict, and model numerically. While very simple closed-form expressions exist to rapidly estimate the temperature increase of a nanoparticle,[49,50] no such expressions have been derived so far for a metal layer. Finally, all the temperature microscopy techniques developed for plasmonics have been used in the case of nanoparticles[40] and were not demonstrated for the case of metal layers, except very recently.[47] This recent interest in photothermal effects for SPR application pressed a deeper description of the underlying photothermodynamics of plasmonic layers.

In this Tutorial, we intend to provide a self-consistent and comprehensive description of the underlying physics of heat generation in metal layers without and with single nanoholes. The two first parts are dedicated to the case of a uniform metal layer under far-field illumination. We first describe the optical absorption physics, and then the heat conduction and temperature increase, discussing the effects of the (adhesion) layer thickness and composition. In the third part, we introduce the theory of the thermoplasmonics of nanoholes based on circular nanohole geometries. We define the concept of absorption cross section for nanoholes and explain the LPR/SPR origin of heat generation. All the results are mainly considering gold as the metal, since it is used in most applications, but the formalism introduced in this Tutorial can be extended to other materials. In particular, several Matlab and Comsol codes are provided in supplementary material for this purpose.

II. ABSORPTION OF LIGHT BY A THIN LAYER

In this introductory section, we recall the optical properties of a metal layer. Due to the simplicity of the system, the physics can be described by simple closed-form expressions based on Fresnel coefficients. We start from the simple case of a single interface and generalize the formalism in the case of a multiple interface system.

A. Fresnel coefficients for a single interface

Let us first consider the system composed of two semi-infinite media, 1 and 2, defined by their complex refractive indices n_1 and n_2 and separated by a planar interface. An incident optical plane wave propagates in medium 1 at an angular frequency $\omega = 2\pi c/\lambda_0$ and with an incidence angle θ_1 on the interface (see Fig. 1). The angle of refraction θ_2 characterizing the optical plane wave in medium 2 is given by the Snell's law $n_1 \sin(\theta_1) = n_2 \sin(\theta_2)$. The reflection r_{12} and transmission t_{12} coefficients, for both a TE (s) and TM (p) polarized plane wave, are given by the Fresnel coefficient[51] that we remind here,

$$r_{12,s} = \frac{n_1 \cos(\theta_1) - n_2 \cos(\theta_2)}{n_1 \cos(\theta_1) + n_2 \cos(\theta_2)}, \quad t_{12,s} = \frac{2n_1 \cos(\theta_1)}{n_1 \cos(\theta_1) + n_2 \cos(\theta_2)},$$
$$r_{12,p} = \frac{n_2 \cos(\theta_1) - n_1 \cos(\theta_2)}{n_2 \cos(\theta_1) + n_1 \cos(\theta_2)}, \quad t_{12,p} = \frac{2n_1 \cos(\theta_1)}{n_2 \cos(\theta_1) + n_1 \cos(\theta_2)}. \tag{1}$$

B. Fresnel coefficients for a two-interface system

We consider now a system composed of three layered media, separated by two planar interfaces, normal to the (Oz) axis. Media 1 and 3 are semi-infinite and the thickness of medium 2 is named h_2. The wave vectors of the plane waves in each media $j \in \{1,2,3\}$ read $\mathbf{k}_j = (k_\parallel, 0, \gamma_j)$, with

$$k_j = 2\pi n_j/\lambda_0, \tag{2}$$

$$k_\parallel = k_1 \sin(\theta_1), \tag{3}$$

$$\gamma_j = \sqrt{k_j^2 - k_\parallel^2}. \tag{4}$$

The reflection and transmission coefficient r_{13} and t_{13} of this three-layer system can be derived by considering a series of multiple reflections inside medium 2, which yields[52]

$$r_{13} = \frac{r_{12} + r_{23}e^{2i\gamma_2 h_2}}{1 + r_{12}r_{23}e^{2i\gamma_2 h_2}} \quad \text{and} \quad t_{13} = \frac{t_{12}t_{23}e^{i\gamma_2 h_2}}{1 + r_{12}r_{23}e^{2i\gamma_2 h_2}}. \tag{5}$$

These expressions are both valid for TE (s) and TM (p) polarized beams by selecting the appropriate s or p coefficients in Eq. (1).

C. Fresnel coefficients for a *m*-layer system

In the case of a m-layer system ($m \geq 4$), the reflection and transmission coefficients can be derived recursively by using the above

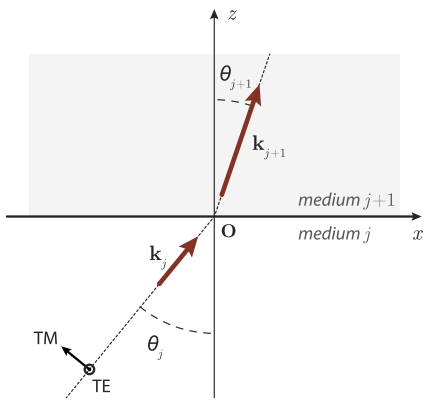

FIG. 1. Representation of the system and definitions of the notations.

expressions (5) and adding new layers one by one. For instance, for a four-layer system, one has

$$r_{14} = \frac{r_{13} + r_{34}e^{2i\gamma_3 h_3}}{1 + r_{13}r_{34}e^{2i\gamma_3 h_3}} \quad \text{and} \quad t_{14} = \frac{t_{13}t_{34}e^{2i\gamma_3 h_3}}{1 + r_{13}r_{34}e^{2i\gamma_3 h_3}}. \tag{6}$$

In the supplementary material, we provide a Matlab code (`Fig2.m`) that enables the computation of Fresnel coefficients for any geometry up to five layers.

D. Transmittance, reflectance, and absorbance

For a m-layer system, the transmission and reflection coefficients in intensity are characterized by the transmittance T_{1m} and reflectance R_{1m} given by

$$R_{1m} = |r_{1m}|^2 \quad \text{and} \quad T_{1m} = \frac{n_m \cos(\theta_m)}{n_1 \cos(\theta_1)}|t_{1m}|^2, \tag{7}$$

with

$$n_1 \sin(\theta_1) = n_m \sin(\theta_m). \tag{8}$$

In the case where $n_1 \sin(\theta_1)/n_m > 1$ (total internal reflection), there is no real solution for θ_m. However, all the above equations are still valid using the exponential definition of the cosine function and the logarithmic definition of the arcsine function, which are both defined for complex numbers.

The absorbance A_{1m}, i.e., the physical quantity of interest in thermoplasmonics applications, is given by

$$A_{1m} = 1 - R_{1m} - T_{1m}. \tag{9}$$

E. Heat generation in a metallic layer

Let us focus on a system composed of two planar interfaces, defining three media characterized by complex permittivities $\varepsilon_i = n_i^2$, $i \in \{1, 2, 3\}$. The thickness of the middle layer is h, and only the middle layer is absorbing to model a dielectric–metal–dielectric system. To simplify the formalism, we will note in this section $n_2 = n$ and $\varepsilon_2 = \varepsilon$. Using a multiple reflection model,[52] the electric field profile within the metallic layer can be simply expressed. In the simplest case of a linearly polarized light at normal incidence, it reads

$$E(z) = E_0 t_{12} \frac{e^{ik_0 nz} + r_{23}e^{ik_0 n(2h-z)}}{1 + r_{12}r_{23}e^{2ik_0 nh}}, \tag{10}$$

where E_0 is the electric field amplitude of the incoming wave from medium 1 at the interface between medium 1 and 2. Then, the heat power per unit volume originating from light absorption within the metal layer can calculated from Eq. (10) using[39]

$$q(z) = \frac{\omega}{2}\mathrm{Im}(\varepsilon)\varepsilon_0|E(z)|^2, \tag{11}$$

where $\varepsilon = n^2$ is the middle layer complex permittivity. Note that the absorption defined by Eq. (9) simply relates to q by

$$A = \frac{1}{I_0}\int_0^h q(z)\mathrm{d}z, \tag{12}$$

where I_0 is the incoming light irradiance,

$$I_0 = n_1 c\varepsilon_0|E_0|^2/2. \tag{13}$$

For a thick enough layer, one can approximate the electric field profile by a single exponential function $E(z) \approx E_0 t_{12} e^{ik_0 nz}$ and extract a simple expression of the heat power density profile,

$$q(z) \approx \frac{\omega}{2}\mathrm{Im}(\varepsilon)\varepsilon_0|t_{12}E_0|^2 e^{-2k_0\mathrm{Im}(n)z}. \tag{14}$$

The exponential decay of this equation yields the expression of the penetration depth in the middle layer, called the skin depth,

$$\delta = \frac{\lambda_0}{4\pi\mathrm{Im}(n)}. \tag{15}$$

Equation (14) is valid for $h \gtrsim 2\delta$. For most metals in the visible range, the imaginary part of the refractive index $\mathrm{Im}(n)$ lies between 3 and 10 giving a skin depth of around 30 nm or less, hence smaller than the usual thickness of the layer. Thus, the heat source density $q(z)$ is highly non-uniform and usually remains localized near the interface facing the incident light beam. Figure 2(a) plots the skin depth for gold.

F. Surface plasmon resonance in a metal layer

A localized plasmon resonance (LPR) is a kind of resonance in illumination wavelength that occurs in plasmonics when the free electrons in the metal are spatially confined, i.e., typically with nanoparticles. The displacement of the free charges from the equilibrium position following the electric field of the incoming light creates a restoring force, attracting the electron back to equilibrium, just like with a mass–spring system, hence the resonance at a particular light frequency.

For a dielectric/metal, no such spatial confinement exists so that no restoring force can happen and no LPR can form. Nevertheless, a dielectric/metal interface remains a popular system in plasmonics because of the possible existence of propagating two-dimensional electromagnetic waves coupled with electronic density oscillation at the interface. These solutions of the Maxwell equations are called surface plasmon polaritons (SPPs) and are characterized by a dispersion relation and a SPP wavelength,[1]

$$k_{\mathrm{SPP}} = \frac{\omega}{c}\sqrt{\frac{\varepsilon_1\varepsilon_2}{\varepsilon_1 + \varepsilon_2}}, \tag{16}$$

$$\lambda_{\mathrm{SPP}} = 2\pi/\mathrm{Re}(k_{\mathrm{SPP}}) \tag{17}$$

$$= \lambda_0 \mathrm{Re}\left(\sqrt{\varepsilon_1^{-1} + \varepsilon_2^{-1}}\right). \tag{18}$$

Values of λ_{SPP} are plotted as a function of the free-space wavelength λ_0 in Fig. 2(b).

Importantly, SPP waves cannot be excited by simply shining light on the metal/dielectric interface. At any wavelength and for any materials, no matter the angle of incidence of the incoming light, it is not possible to fulfill the equality condition $k_{\parallel}^{\mathrm{light}} = k_{\mathrm{SPP}}$ between the in-plane component $\mathbf{k}^{\mathrm{light}}$ of the wave vector of the incoming light beam and k_{SPP}. There exist two common approaches to lift this limitation arising from a mismatch of wave vectors. The first one consists of breaking the translational symmetry of the system by adding a localized perturbation: a nanoaperture in the layer (the topic of this

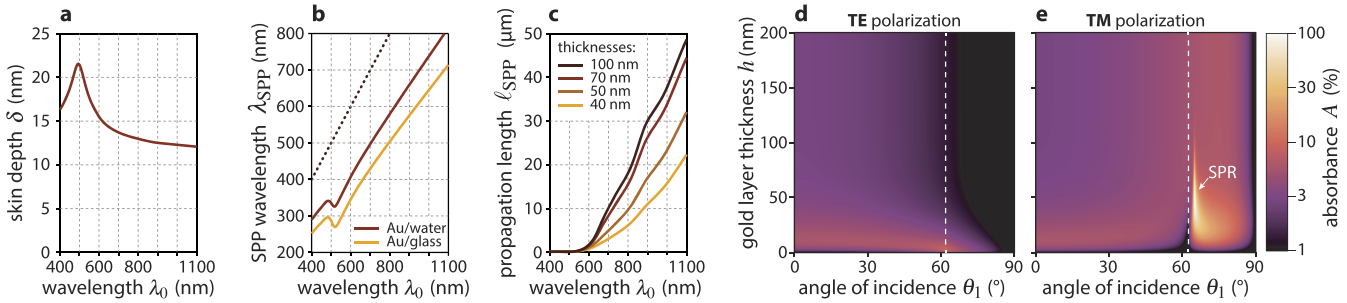

FIG. 2. (a) Skin depth of gold. (b) SPP wavelength of a gold/dielectric interface as a function of the free-space wavelength $\lambda_0 = 2\pi c/\omega$. The cases of glass and water are represented. The dotted line represents the free-space wavelength λ_0, as a comparison. (c) Propagation length of a SPP of a water/Au/glass system as a function of the wavelength for four different Au layer thicknesses. (d) and (e) Absorbance of a gold layer on glass for TE and TM polarization at $\lambda = 900$ nm, as a function of the layer thickness and incidence angle. Calculations conducted using Eqs. (1)–(9). Optical constants for the gold layer are taken from Ref. 53.

tutorial, see later on), a nanoparticle lying on the metal layer, or any nanostructuration on the metal film (roughness, grating), which will act as a coupler between the far-field illumination and the SPP. Second, without breaking the translational symmetry, the excitation of a SPP at one interface can be achieved with far-field illumination if another metal/dielectric interface enters into play at close proximity, i.e., if a metal *layer* is considered (also the topic of this tutorial). With a metal layer (medium 2) embedded in two dielectric media (1 and 3), a SPP at the 2/3 interface can be excited if shining light from medium 1, only with a TM illumination (not TE) and, importantly, only if $n_1 > n_3$. Moreover, excitation of SPP fulfilling all these conditions occur at a specific resonance incident angle $\theta_1 = \theta_{SPR}$ such that in the first approximation,[54,55]

$$\sin\theta_{SPR} \approx \mathrm{Re}\left(\frac{1}{n_1}\sqrt{\frac{\varepsilon_2\varepsilon_3}{\varepsilon_2+\varepsilon_3}}\right). \tag{19}$$

This picture leads to the concept of surface plasmon resonance (SPR). Let us recall that only ε_2 possesses an imaginary part in this expression. Depending on the wavelength, typical θ_{SPR} angles lie in the range 64°–72° for a glass–gold–water system, the longer the wavelength, the smaller the incidence angle.[55] Note that this expression is independent of the metal thickness h_2. The metal thickness only affects the efficiency of the plasmonic excitation, with a maximum around $h_2 = 50$ nm for gold [see Fig. 2(e)]. Illuminating a metal layer from the high-refractive index dielectric side can be achieved using various configuration: in particular, (i) using high numerical aperture (NA), oil-immersion objective lenses, by focusing the laser at the back focal plane of the objective and laterally shifting it (the NA has to be larger than $n_1 \sin\theta_{SPR}$), and (ii) using a prism as medium 1, like in the so-called Kretschmann configuration.

An important feature of a SPP is its propagation length ℓ_{SPP}. For a very thick layer, it is simply related to the imaginary part of the SPP wave number, like for any wave: $L_{SPP} = \mathrm{Im}(k_{SPP})/2$. For small layer thicknesses, comparable with the skin depth, the SPP propagation is damped. Unlike the SPP wavelength or wave number, the propagation length is thus quite dependent on the layer thickness in the range 0–100 nm. It can be written as (see the Appendix of Ref. 54)

$$\ell_{SPP} = \frac{1}{2}\mathrm{Im}\left(\frac{1}{k_{SPP}+\delta k(h)}\right), \tag{20}$$

where

$$\delta k(h) = \frac{r_{12,p}e^{2i\alpha(h)}}{\varepsilon_3-\varepsilon_2}\frac{2\omega}{c}\left(\frac{\varepsilon_2\varepsilon_3}{\varepsilon_2+\varepsilon_3}\right)^{3/2}, \tag{21}$$

with

$$\alpha(h) = \frac{\omega}{c}\frac{\varepsilon_2}{\sqrt{\varepsilon_2+\varepsilon_3}}h, \tag{22}$$

$$r_{12,p} = \frac{(a-i\varepsilon_1)^2}{a^2+\varepsilon_1^2}, \tag{23}$$

$$a = \mathrm{Re}(\varepsilon_2)(1-\varepsilon_1)-\varepsilon_1. \tag{24}$$

Here, $\delta k(h)$ vanishes for thick layers ($h \to \infty$). However, for thin layers, its imaginary part tends to reduce the propagation length ℓ_{SPP}. The SPP cannot loose energy by radiation toward medium 3. However, the proximity of the 1–2 interface enables light radiation toward medium 1, hence the reduced propagation length. The propagation length spectrum for a glass–gold–water system is plotted in Fig. 2(c) for various layer thicknesses. Above 100 nm, the layer behaves as an infinitely thick medium.

Experimentally, this theoretical expression of the propagation length matches well experimental measurements, provided the metal layer is crystalline. If the metal layer is polycrystalline/amorphous or rough, then this propagation length is reduced.[56–58] For instance, for gold, Kuttge *et al.* used cathodoluminescence imaging spectroscopy to excite and measure ℓ_{SPP} for crystalline and polycrystalline gold layers.[56] A reduction of the propagation length of around a factor of 3 was evidenced in the infrared range.

Close to the resonance angle θ_{SPR}, the system demonstrates reduced reflectivity of the light beam and an increase in light absorption. Figures 2(d) and 2(e) present numerical simulations related to a textbook case in plasmonics: a gold layer on glass and in contact with water, where the angle of illumination and the thickness of the layer are varied. Only with a TM, polarization and at a specific angle of incidence, a surface plasmon can be excited, as noticed by an increase in the absorbance [Fig. 2(e)]. The excited SPP propagates on the metal/water interface, while the light illuminated the glass/water interface. No SPP excitation can be achieved when illuminating the system from the lower refractive index medium (air in our case). The reduced reflectivity at a very specific angle due to absorption is at

the basis of a famous application called SPR biosensing, dating from the 1990s,[59] one of the rare applications of plasmonics that achieved widespread commercialization.

G. Effect of the adhesion layer

Gold poorly adheres on glass. To achieve stable plasmonic samples made of gold on glass substrates, a thin adhesion layer is often required to avoid detachment of the gold structures or layer during use. This adhesion layer usually consists of a few-nanometer-thick layer of chromium or titanium.[60] Unfortunately, such metals have poor optical properties, damping the plasmon resonance, and exhibit significant optical absorption in the whole visible-IR range, stronger than gold, as demonstrated in Figs. 3(a)–3(c). The simulations are here conducted at normal incidence for the sake of simplicity and because it is sufficient to derive the main conclusions. In particular, Fig. 3(b) shows that Cr and Ti layers absorb around four times more than gold in the visible range at equal thickness. This ratio increases even more in the infrared, as shown in Fig. 3(c). In any case, the absorption of Ti, Cr, and Au layers saturates above 10 nm thickness. Figures 3(d) and 3(e) are striking, as they show that the absorption of a Cr–Au layer is quite constant, around 50% for 5 nm Cr, no matter the thickness of gold that is put on top, meaning that the absorption is mainly due to the Cr layer and that the Au layer has no effect on the absorption. This statement is less true in the IR range, as shown in Fig. 3(f). The absorption is no longer constant upon adding gold on top of a 5 nm Cr layer. However, surprisingly, the addition of gold on top of a 5 nm thick Cr layer reduces the absorption, down to a factor of 2. This phenomenon of adding the material but decreasing the absorbance is also observed, albeit less pronounced, with single metallic layers, as can be seen in Figs. 3(b) and 3(c), where the absorption of a gold, chromium, or titanium layer shows a local absorbance maximum for a layer thickness around 10 nm. This observation means that the absorption behavior of a metallic layer is not intuitive and requires modeling and computation even for simple systems.

Figures 3(g)–3(i) address the effect of the illumination side. Whether the illumination impinges on the adhesion layer side or on the opposite side changes much the absorption, as expected. When illuminating from above (the opposite side of the adhesion layer), the adhesion layer has no effect on the absorbance property of the system.

To give an idea of the temperature increase, a 5 nm Cr + 100 nm Au thin layer excited with a 1 mW focused laser beam experiences a 3.6 °C temperature increase when excited at 600 nm and 1.4 °C when excited at 900 nm, which can easily become an issue for SPR-based sensors[61] [calculations obtained using the `Temperature_layer.mph` Comsol code provided in the supplementary material (see Sec. III B for more details)]. A temperature

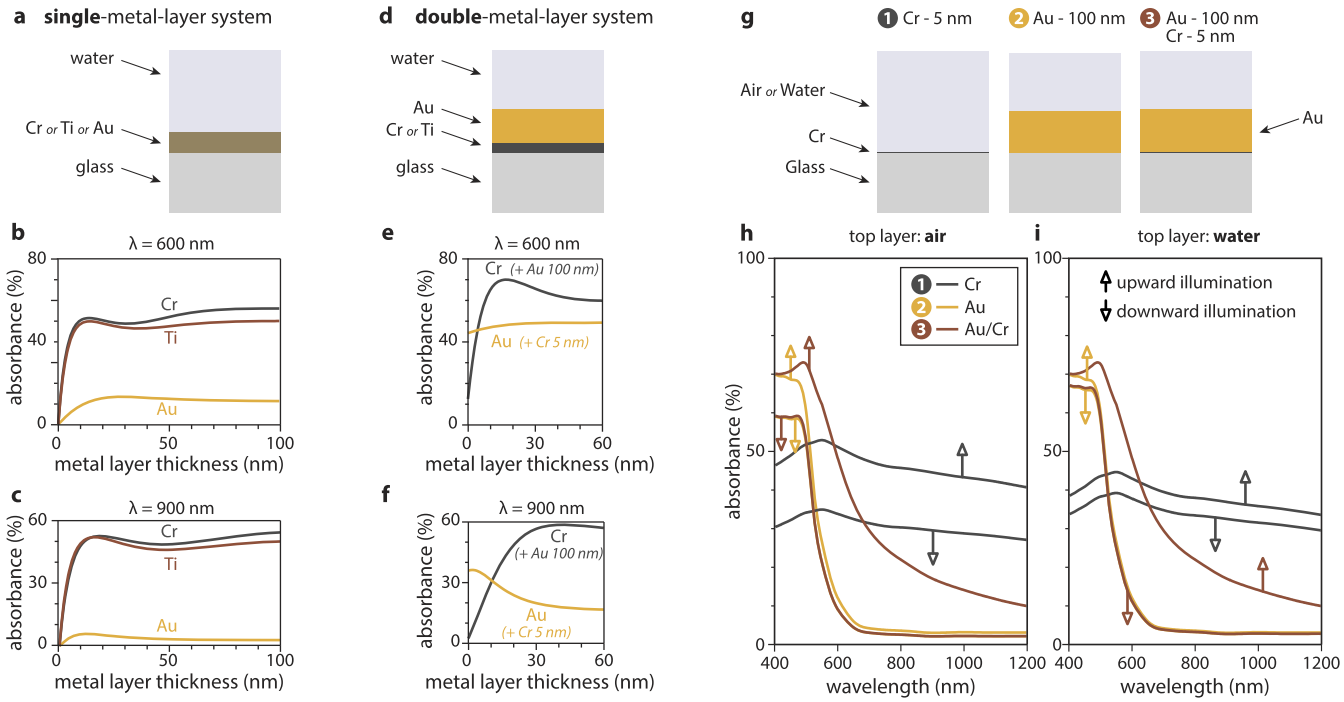

FIG. 3. (a) Schematic of a single-metal-layer system related to (b) and (c). (b) Absorption of a single-layer system at $\lambda = 600$ nm. (c) Absorption of a single-layer system at $\lambda = 900$ nm. (d) Schematic of a two-metal-layer system related to (e) and (f). (e) Absorbance of a two-layer system, at $\lambda = 600$ nm, as a function of the Cr layer thickness (dark gray curve, the Au layer thickness being maintained at 100 nm) and as a function of the Au layer thickness (yellow curve, the Cr layer thickness being maintained at 5 nm). (f) Same as (e) for $\lambda = 900$ nm. (g) Schematics of the systems related to images (h) and (i): (1) A 5-nm thick chromium layer, (2) a 100-nm thick gold layer, and (3) and 100-nm thick gold layer on top of a 5 nm thick chromium layer. (h) Absorbance as a function of the wavelength for the three systems, when the upmost layer is air, and for upward and downward illumination. (i) Same as (h) when the upmost layer is water.

increase can be detrimental for some applications. There exist some possibilities to limit this temperature increase. The first one is to reverse the excitation side and shine the sample from the water/air side. In this case, the gold layer blocks the incident light and prevents it from heating the adhesion layer, as shown in Fig. 3.

In case excitation has to come from the glass side, to excite surface plasmon polaritons (SPPs), for example, it is possible to use other adhesion layers such as TiO_2, Cr_2O_3,[62] and Ge[63] in order to reduce the absorbance of the adhesion layer[64] or even totally suppress it using a mercaptosilane molecular layer.[65,66]

III. HEAT TRANSFER IN A METAL LAYER

Section II was focused on how much light is absorbed by a metal layer system. This section rather focuses on how this amount of thermal energy diffuses in this system. The presence of a metal layer, that is, a highly thermally conductive film, makes the thermal diffusion highly anisotropic and more complicated to describe compared with the usual case in thermoplasmonics of a nanoparticle.

In this section, we consider a thin, infinite metal layer (subscript label "2") of thickness h sandwiched between two semi-infinite media, one labeled "1" located at $z < 0$ and the other labeled "3" located at $z > h$. We consider the problem invariant by rotation around the (Oz) axis. We shall use the polar coordinates: $\mathbf{r} = (r, \theta, z) = (\boldsymbol{\rho}, z)$ and define $\rho = |\boldsymbol{\rho}|$.

A. Exact solution of the steady-state heat diffusion equation

In the above-described system, the general heat diffusion equation in the steady state reads[40]

$$-\nabla \cdot [\kappa(\mathbf{r}) \nabla T(\mathbf{r})] = q(\mathbf{r}). \tag{25}$$

Here, T is the temperature, q is the heat power density (power per unit volume), coming from light absorption, and κ is the thermal conductivity. Equation (25) can be recast for the three layers into

$$\nabla^2 T = 0 \quad \text{for } z > h, \tag{26}$$

$$-\kappa_2 \nabla^2 T = q \quad \text{for } z \in [0, h], \tag{27}$$

$$\nabla^2 T = 0 \quad \text{for } z < 0, \tag{28}$$

with the boundary conditions of temperature T continuity and heat flux density $\mathbf{J} = -\kappa \nabla T$ continuity at the $z = 0$ and $z = h$ interfaces.

This set of Eqs. (26)–(28) has no closed-form solution. There exist, however, integral expressions for a point-like source of heat, i.e., Green's functions, solutions of the equation[67]

$$-\nabla \cdot [\kappa(\mathbf{r}) \nabla G(\mathbf{r})] = \delta(\mathbf{r}_s). \tag{29}$$

The general solution is given in Refs. 40 and 67. In the case of a point-like source located in the middle layer, the Green's function for $\mathbf{r}$ in the middle layer reads

$$G(\mathbf{r}, \mathbf{r}_s) = \frac{1}{4\pi\kappa_2 \sqrt{|\boldsymbol{\rho} - \boldsymbol{\rho}_s|^2 + (z - z_s)^2}} + \frac{1}{4\pi\kappa_2} \int_0^\infty \frac{(\kappa_2 - \kappa_3)(\kappa_2 - \kappa_1) e^{-u(2h + z_s - z)} + (\kappa_2 - \kappa_3)(\kappa_2 + \kappa_1) e^{-u(2h - z_s - z)}}{(\kappa_2 + \kappa_3)(\kappa_2 + \kappa_1) + (\kappa_2 - \kappa_1)(\kappa_3 - \kappa_2) e^{-2uh}} J_0(|\boldsymbol{\rho} - \boldsymbol{\rho}_s| u) \, \mathrm{d}u$$
$$+ \frac{1}{4\pi\kappa_2} \int_0^\infty \frac{(\kappa_2 - \kappa_1)(\kappa_2 + \kappa_3) e^{-u(z_s + z)} + (\kappa_2 - \kappa_3)(\kappa_2 - \kappa_1) e^{-u(2h + z - z_s)}}{(\kappa_2 + \kappa_3)(\kappa_2 + \kappa_1) + (\kappa_2 - \kappa_1)(\kappa_3 - \kappa_2) e^{-2uh}} J_0(|\boldsymbol{\rho} - \boldsymbol{\rho}_s| u) \, \mathrm{d}u. \tag{30}$$

Equation (30) can be computed analytically, as demonstrated in the Mathematica Notebook (μGreen_T_3layer.nb) provided in the supplementary material. Figures 4(b) and 4(c) display numerical simulations of the temperature profile from a point-like heat source in uniform media (gold or glass) and in a metal layer embedded in glass. We considered $\kappa_{glass} = 1$ W m^{-1} K^{-1} and $\kappa_{gold} = 310$ W m^{-1} K^{-1}. For the uniform geometries (cases 1 and 3), the temperature profile simply reads $T(\rho) = Q_0/4\pi\kappa_i\rho$. Case 2 requires the use of Eq. (30), and Figs. 4(b) and 4(c) show that, at short distance, the temperature profile follows the one of a uniform metal space, while far from the heat source, above around 100 times the thickness of the metal, one retrieves exactly the temperature profile of the uniform space with the glass thermal conductivity. This result counter-intuitively shows that the presence of a metal layer does not affect the temperature profile at long distance. It only damps it over a finite distance. It is tempting to look for a simplification of Eq. (30), e.g., at the first order in κ_1/κ_2 and κ_3/κ_2, as the ratio is around 1/300. However, we do not recommend this simplification, which yields fully wrong results, according to our numerical simulations. Completely neglecting κ_1 and κ_3 is, however, justified when working with a suspended layer, as shown further on.

Equation (30) can naturally be used to compute the temperature for more realistic, extended sources of heat (no longer point-like), for instance, originating from a focused laser. In that case, the heat source density within the metal layer can be approximated by the function $q_{layer}(z)$ [see Eq. (11)] multiplied by a 2D normalized Gaussian profile,

$$q(\mathbf{r}) = \frac{1}{2\pi\sigma^2} e^{-\rho^2/2\sigma^2} q_{layer}(z), \tag{31}$$

where 2σ is the beam waist. Such a heat source distribution is shown in Fig. 4(e) in the case of a 50-nm thick gold layer.

Then, to compute the temperature profile resulting from this heat source density, one can use a convolution method. Before doing so, let us first derive some simplifications. Equation (30) obeys two important properties. First, it obeys the relation

$$G(\mathbf{r}, \mathbf{r}_s) = G(|\boldsymbol{\rho} - \boldsymbol{\rho}_s|, z, z_s). \tag{32}$$

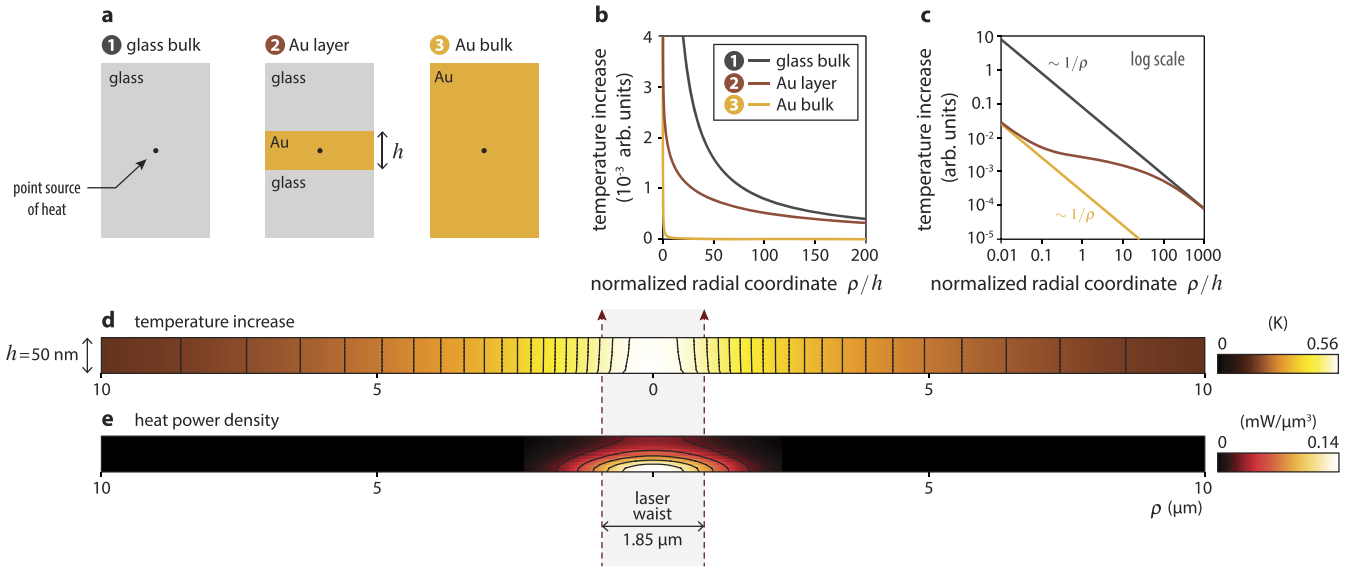

FIG. 4. (a) Schematics of three geometries heated by a point-like source of heat. (b) Numerical simulation of the radial profile of the temperature increase for the three cases depicted in (a). (c) Same data as (b) in log–log scale. (d) Numerical simulation of the temperature distribution in the (ρ, z) plane within a 50-nm-thick gold metal layer, glass below, water on top, illuminated by a focused 1 mW laser beam, at $\lambda = 1064$ nm, focused by a 0.7 NA objective. (e) Associated heat power density $q_{\text{layer}}(\rho, z)$. Simulations conducted using the three-layer Green's function formalism [Eq. (30)].

This property comes from the invariance of the system by translation in the x–y plane. Thus, it is not necessary to specify a particular radial position $\boldsymbol{\rho}_s$ of the heat source, which can be set as $\boldsymbol{\rho}_s = 0$. Second, interestingly, by variable substitution $v = uh$ in Eq. (30), one can evidence that the Green's function verifies the property

$$G(\rho, z, z_s) = \frac{1}{h} G\left(\frac{\rho}{h}, \frac{z}{h}, \frac{z_s}{h}\right). \tag{33}$$

As a consequence, it is not necessary to compute a new set of Green's functions for each new layer thickness. A set of N^2 1D-Green's functions suffices

$$G_{t,s}(\rho) = G(\rho, z_t, z_s), \quad (t, s) \in [\![1, N]\!]^2, \tag{34}$$

where N is the number of discretization layers along the z direction, with the metal layer. Such a set a Green's function for $N = 20$ was computed using the Mathematica solver (see the Mathematica Notebook μGreen_T_3layer.nb in the supplementary material). Then, these Green's functions (30) can be used to determine the temperature for any thickness h, at any height z_t in the metal layer, and for any heat source density distribution q using

$$T(\boldsymbol{\rho}, z_t) = \sum_{s=1}^{N} \int \frac{1}{h} G_{t,s}\left(\frac{|\boldsymbol{\rho} - \boldsymbol{\rho}_s|}{h}\right) q(\boldsymbol{\rho}_s, z_s) \mathrm{d}\mathbf{r}_s. \tag{35}$$

Figure 4(d) displays the result of a temperature distribution calculated using Eq. (35). This profile corresponds to a 50-nm gold film between glass and water, illuminated at 1064 nm (a common laser wavelength used in nanohole plasmonics[68]) by a focused laser beam (NA 0.7). These calculations evidence that the temperature spreads much in the z direction within the metal layer, making it almost uniform in z, although the heat source is not.

B. Using Comsol for thermoplasmonics simulations

Using Comsol can also be an efficient approach to model such a system, provided some pitfalls are avoided, in particular, regarding the boundary conditions. The $1/r$ decay of the temperature in a dense medium, which is a slow decaying function, implies that the temperature usually does not exactly reach zero in the boundary of the modeled system, no matter how far the boundary is set.

The case of a nanoparticle in a uniform medium is instructive, although it is not the subject of interest of this Tutorial. If the nanoparticle is spherical, using Comsol is not necessary to compute any temperature profile because the large thermal conductivity of the nanoparticle yields to the assumption that the heat source density can be considered as uniform within the nanoparticle of volume V and equal to $q = \sigma_{\text{abs}} I/V$, and the problem has a closed-form expression in the surrounding medium that reads $T(r) = \sigma_{\text{abs}} I/4\pi\kappa r$.[39,49] The use of Comsol becomes relevant for nanoparticles of arbitrary geometries. To compute the temperature profile using Comsol, one can still assume $q = \sigma_{\text{abs}} I/V$ uniform. The critical feature concerns the boundary conditions. The natural idea consists in placing the boundary far enough and set it to room temperature. However, the slowly decreasing temperature profile $1/r$ causes problem. Even when setting the boundaries at a distance that is ten times the radius of the particle, it yields a temperature underestimation of 10%. Another possible solution, *a priori*, consists in setting the outer flux instead of the temperature at the boundary of the domain because in the steady state, the integral of this flux over the boundary must be equal to the power delivered by the particle qV. However, in practice, it does not converge as even an infinitely small difference between qV and the integrated flux yields a divergence. We rather propose two methods to properly set the boundary conditions in thermal

simulation of heated nanoparticles. Method 1 consists in defining a spherical system boundary with temperature boundary conditions set as uniform and equal to $T_{\text{boundary}} = T_{\text{ambient}} + \sigma_{\text{abs}} I/4\pi\kappa R_{\text{d}}$, where R_{d} is the radius of the spherical domain. Indeed, far from the nanoparticle (couple of nanoparticle sizes), the temperature profile varies as $1/r$ and is no longer affected by the particular geometry of the nanoparticle. Method 2 requires the heat transfer module (not the built-in one), which offers the use of infinite domains. Such domains have to be placed at the boundary of the system.[69]

Let us now focus on COMSOL thermal computation involving infinite metal layers. The slow $1/r$ decay problem mentioned in the previous paragraph is even more significant here due to the fast heat diffusion through the metal layer, which makes the temperature decay even slower [see Fig. 4(b), case 2]. Let us explain to what extent the two above-mentioned methods can be applied to metal layers. Method 1: The plasmonic system necessarily reaches here the boundary of the system, making Method 1 *a priori* ineffective. However, Fig. 4(c) suggests an efficient trick to make it effective. Since the temperature eventually reaches the uniform bulk temperature at large ρ, it suffices to consider the boundary far enough, at least at $\rho = 100h$, make it spherical (with a radius R_{d}), and set its temperature to $T_{\text{boundary}} = T_{\text{ambient}} + P_0/(4\pi\bar{\kappa}R_{\text{d}})$, where $\bar{\kappa} = (\kappa_1 + \kappa_3)/2$. Using this caution, Comsol simulations become accurate and perfectly correspond to Green's function simulations. Figure 5 compares Green's function simulations, COMSOL simulations for a 100 nm thick gold layer, with a Cr adhesion layer, heated at 790 nm from the top (water side) or from below (glass slide). In any case, the match between Comsol and Green's function is perfect. The Comsol and Matlab programs are provided in the supplementary material (`Temperature_layer.mph`, `Fig4.m`). Method 2, requiring the use of the heat transfer module, was found also effective with metal layers. Meshing infinite domains has to be done with caution, but it enables one to use much smaller computation domains. The code `Temperature_nanohole.mph` provided in the supplementary material makes use of infinite domains.

In Fig. 5, we also take the opportunity to show experimental measurements performed on this exact system. The correspondence looks good, supporting the effectiveness of the numerical approaches we propose here. The only free parameter was for Fig. 5(c) the Cr layer thickness, which was not known precisely, and had to be set to 6.05 nm, a value within the experimental uncertainty of 5 ± 2 nm. This good match also confirms that using the bulk gold permittivity[53] and gold thermal conductivity is still justified, despite the nanometric dimension of the system and the presence of interfaces. It has been shown in plasmonics that using the bulk permittivity of gold was fine for nanoparticles, provided their dimensions are not smaller than a few nanometers.[70–72] Below a few nanometers, surface effects[70,71] and nonlocal effects[72] may become dominant, making the use of the bulk permittivity in simulation not accurate. The same rule certainly applies for gold layers and their thicknesses. In addition, the thermal conductivity of the adhesion layer may strongly differ from the bulk conductivity due to the very small thickness and roughness of the layer. However, the adhesion layer is so small compared with the gold layer that its contribution to thermal diffusion is negligible anyway.

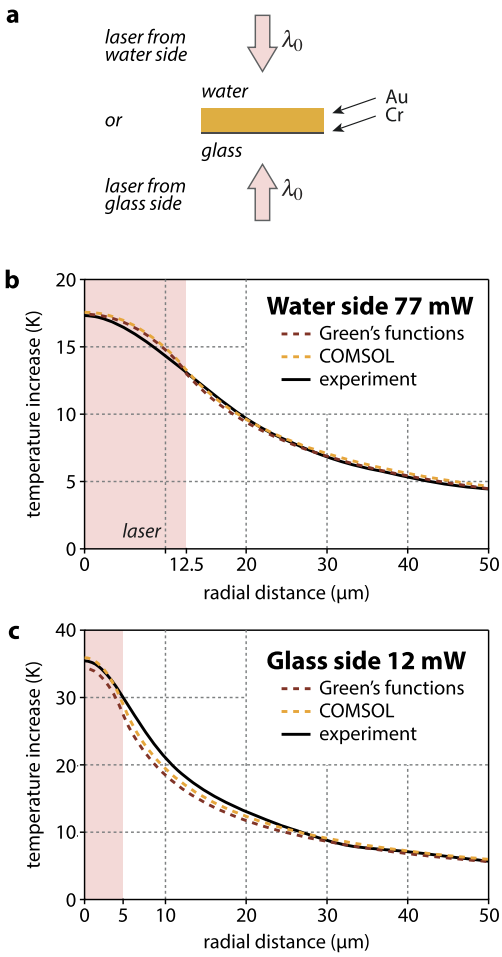

FIG. 5. Comparison between numerical simulation (COMSOL and Green's functions) and experimental measurements of the temperature profile of a gold film under illumination by a uniform laser beam at $\lambda = 790$ nm. (a) Schematic of the system, consisting of a 100 nm gold layer, supported on a 5 nm thick Cr adhesion layer, illuminated either from the top or from below. (b) Temperature profiles for the case of top illumination, with a beam diameter of 25 μm. In that case, the Cr layer has no effect on the light absorption. The models did not consider it. Experiments were conducted with a 40× water immersion objective. (c) Temperature profiles for the case of bottom illumination, with a beam diameter of 9.5 μm. The Cr layer thickness was used as a free parameter, set to 6.05 nm, a value fully consistent with the estimation. Experiments were conducted with a 100× oil-immersion objective.

C. What is the temperature increase of a metal film under illumination?

The question raised in the title of this subsection is what eventually matters, but the answer is not unique. Many parameters come into play, such as the beam size, beam power, multilayer materials, wavelength, layer thickness, and angle of incidence. In the frame of this subsection, we will focus on the most typical case of a gold layer on top of glass, covered with water, illuminated using a focused laser beam of $P = 1$ mW, at normal incidence. This configuration lets us with only two free parameters: the layer thickness h and the wavelength λ, and offers thus the possibility to answer the initial question with 2D maps, as shown in Fig. 6. Any other configuration than

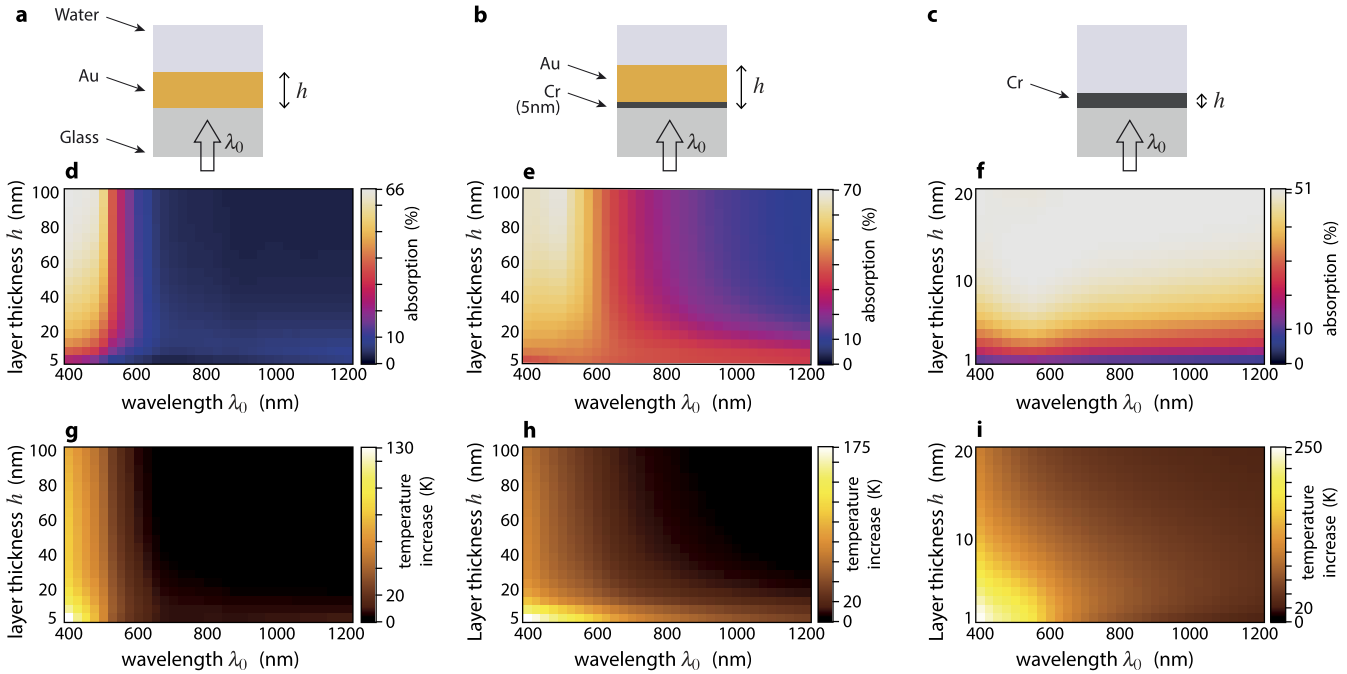

FIG. 6. (a)–(c) Three layer systems studied numerically, namely, a single Au layer (a), a Au/Cr layer (b), and a Cr layer (c), deposited on glass and covered with water and illuminated by a focused laser of power $P = 1$ mW. (d) Absorption of the layer as a function of the wavelength and layer thickness, corresponding to the geometry (a). (e) Same as (d) for the geometry (b). (f) Same as (d) for the geometry (c). (g) Maximum temperature increase in the layer as a function of the wavelength and layer thickness, corresponding to the geometry (a). (h) Same as (h) for the geometry (b). (i) Same as (g) for the geometry (c).

the one presented here can be modeled using the codes provided in the supplementary material (Fig6def.m and Fig6ghi.m). Figure 6 evidences the strong absorption of gold layers for wavelengths typically below 550 nm due to the onset of interband absorption. Above this wavelength threshold, photon absorption is strongly reduced because of the low energy photon that prevents authorized (interband) transitions and because of the perfect translation invariance of the system. Above a certain thickness, on the order of the skin depth (see Fig. 2), the fraction of absorbed light is quite constant. However, the temperature markedly drops upon thickening the layer, as the heat has to spread over a larger volume. The main conclusion from these data is that heating a gold layer in the red-infrared range, even upon focalizing the beam, remains unlikely when using reasonable laser powers. Importantly, this conclusion holds as long as an adhesion layer is not introduced: Figs. 3(h) and 3(i) display results related to the introduction of a Cr adhesion layer between the glass and the gold substrates. The effect of an adhesion layer is to strongly raise the absorption in the red-infrared range, where the absorption used to be almost nonexistent with a pure gold layer. Experimentally, when temperature increase is to be avoided, it is thus preferable to shine the other face of the metal layer (see Fig. 3).

D. Suspended layer in the steady state

Let us consider a uniform layer of thermal conductivity κ and suspended in vacuum. This situation may occur in plasmonics experiments conducted in the vacuum chamber of an electron microscope, coupled with laser illumination, and using a TEM (transmission electron microscope) grid, for instance. In this case, heat generated by laser absorption can only escape in two dimensions, that is, much less efficiently than in three dimensions. Equation (27) now becomes

$$-\frac{\kappa}{\rho}\frac{\partial}{\partial\rho}\left(\rho\frac{\partial T}{\partial\rho}\right) = \frac{Q_0}{h}\delta(\boldsymbol{\rho}), \tag{36}$$

where Q_0 is the power delivered into the layer. The general solution of this Poisson's equation reads

$$T(\rho) = -\frac{Q_0}{2\pi\kappa h}\ln(\rho) + C, \tag{37}$$

where Q_0 is the power delivered in the middle layer and C is a constant of integration. κh can be seen as a two-dimensional thermal conductivity. This logarithmic profile looks non-physical at first glance because it does not tend toward 0 for $\rho \to \infty$ and, thus, cannot correspond to any physical situation. This dependence simply means that heating a true two-dimensional system does not yield a steady state: the heat is to be delivered more rapidly than how fast it can escape. Experimentally, the consequence is that even the use of a weakly absorbent layer and a moderate laser intensity can easily generate a dramatic temperature increase or even a blast of the metal film or the TEM grid. This phenomenon has already been observed experimentally for AFM cantilevers operating under vacuum despite a highly reflecting gold-coating and a low irradiation intensity (<1 mW).[73] In practice, what regulates the temperature increase in such conditions is the heat leak occurring at the place where the layer is

attached to a bulk holder. The closer the holder, the lesser the temperature increase. Hence, the nature of the holder unexpectedly is of primary importance for suspended layers.

E. Suspended layer and transient heat transfer

Illuminating a suspended layer does not necessarily yield catastrophic photothermal effects. When considering a single pulse of light, the temperature increase can be moderate if the pulse duration is short enough. Let us investigate in detail this question.

For a 2D system, there exists a closed-form solution of the transient heat diffusion equation with a Dirac excitation. The equation reads

$$\mu c_p \frac{\partial T}{\partial t} - \frac{\kappa}{\rho}\frac{\partial}{\partial \rho}\left(\rho \frac{\partial T}{\partial \rho}\right) = \frac{E_0}{h}\delta(\boldsymbol{\rho})\delta(t), \tag{38}$$

and the exact solution is

$$T(\rho, t) = \frac{E_0}{4\pi h \kappa t}\exp\left(-\frac{\rho^2}{4Dt}\right), \tag{39}$$

where $D = \kappa/\mu c_p$ is the thermal diffusivity of the layer. Equation (39) differs from the three-dimensional (3D) case[74] by the $1/t$ pre-factor, which reads $1/t^{3/2}$ in 3D. This solution can be understood as the Green's function $G(\rho, t)$ associated with Eq. (38) such that $T(\rho, t) = E_0 G(\rho, t)$,

$$G(\rho, t) = \frac{1}{4\pi h \kappa t}\exp\left(-\frac{\rho^2}{4Dt}\right). \tag{40}$$

Then, this Green's function can be used to numerically calculate any temperature distribution following a more realistic, spatially spread laser beam. One just has to use a convolution,

$$T(\rho, t) = \iint e_0(\boldsymbol{\rho}')G(|\boldsymbol{\rho} - \boldsymbol{\rho}'|, t)\mathrm{d}\boldsymbol{\rho}', \tag{41}$$

where $e_0(\boldsymbol{\rho})$ is the absorbed fluence (deposited/absorbed energy per unit area). Let us solve this equation for the simple case of a top-hat fluence profile of area S: $e_0(\rho) = E_0/S$ for $\rho < \sqrt{S/\pi}$ 0 otherwise. At time $t = 0$, there exists a simple closed-form solution of the equation, noticing that $\lim_{t\to 0} G(\rho, t) = \delta(\boldsymbol{\rho})/(h\mu c_p)$. Equation (41) thus simply yields a uniform temperature increase confined with the radius $\rho < \sqrt{S/\pi}$,

$$T(\rho, 0) = e_0/h\mu c_p = E_0/Sh\mu c_p = E_0/V\mu c_p = E_0/C_p, \tag{42}$$

where C_p is the volumetric heat capacity of the illuminated volume of the suspended layer. This expression makes sense since $E_0/V\mu c_p$ is indeed the temperature increase supposed to occur when depositing an energy E_0 in a volume V of volumetric heat capacity μc_p. Since this deposited energy E_0 results from the absorption of a pulse of light, one can write $E_0 = AP_{\text{laser}}\tau_{\text{laser}}$, where A is the layer absorbance [to be calculated using (9)], P_{laser} is the laser power, and τ_{laser} is the duration of the pulse. Importantly, this estimation of the temperature increase is valid only if the pulse duration τ_{laser} is shorter than the diffusion time within the layer, which is $\tau_D = S/D$. If the pulse duration is longer, then diffusion occurs concomitantly during the absorption, and the actual temperature increase is reduced compared with this simple estimation. Note that this initial temperature increase is not dependent on the thermal conductivity of the layer, which may be counterintuitive: using highly conductive layer, like metal, does not help reducing the temperature increase. To reduce any detrimental temperature increase, the important parameters to consider are just the volumetric heat capacity of the material and the thickness of the layer, which both contribute to damp the temperature elevation when increased.

Let us derive some orders of magnitude, with the example of a suspended 100-nm thick gold layer. Equation (9) (i.e., code `Fig2.m` in the supplementary material) gives $A = 0.0819$ for a wavelength of $\lambda = 800$ nm. Assuming $S = \lambda^2$ to model a focused laser, giving a thermal diffusion time $\tau_D = 5$ ns, a laser power of $P_{\text{laser}} = 1$ mW, and a pulse duration of $\tau_{\text{laser}} = 1$ ns, one finds a temperature increase of $T(0,0) = 0.5\,^\circ$C. When using a pulsed laser, P_{laser} is the peak power, not the average power that would be measured with a powermeter. When using a pulsed laser with a given repetition rate, then the layer will have to release a continuing input of light energy, and a higher temperature increase compared with the $T(0,0)$ can be achieved if the repetition rate is high enough. To determine this temperature increase, the time average laser power (the one measured with a powermeter) has to be considered and the discussion of Sec. III D has to be applied as if the laser were in a continuous mode.

When considering a system with restricted heat diffusion pathways like here, thermal radiation may become an important heat release modality *a priori*, and this question is worth investigating here. The power loss by radiation of body of absolute temperature T and surface S is given by the Stefan–Boltzmann law

$$j = SA\sigma_{SB}\left(T^4 - T_0^4\right), \tag{43}$$

where $\sigma_{SB} \approx 5.67 \times 10^{-8}$ W/m^2 K^4 is the Stefan–Boltzmann constant, where A is the emissivity or, equivalently, the absorptivity of the material ($0 < A < 1$), not at the laser wavelength but at the thermal emission wavelength, usually located in the infrared. The emissivity of metals are extremely weak in the infrared, where metals are rather transparent ($A < 0.01$ for gold).[75] Equation (43) gives a radiated power in the pW range [for $S \sim (1\,\mu\text{m})^2$], completely negligible compared with the mW power that is flowing through the suspended layer ($j \sim hT\kappa$). Consequently, even with suspended layers, thermal radiation is far from being a possible pathway for energy release. Note that caution has to be used with Eq. (43). For radiating surfaces that have a subdiffraction area, the area S is Eq. (43) does not make much sense anymore. This issue is encountered with nanoparticles, for instance. The expression of the radiated energy by a nanoparticle no longer involves any surfaces and emissivity/absorptivity. It simply involves the absorption cross section of the nanoparticle (see Ref. 40, p. 213).

The transient evolution originating from a step function [$q(t < 0) = 0$ and $q(t > 0) = Q_0\delta(\boldsymbol{\rho})/h$] is also of interest. The solution is obtained by integrating Eq. (39),

$$T_m(r, t) = \frac{Q_0}{4\pi h\kappa}\int_0^t \frac{1}{t'}\exp\left(-\frac{r^2}{4Dt'}\right)dt'. \tag{44}$$

With the variable substitution $u = r^2/\sqrt{4D_m t'}$ and using the exponential integral function defined as

$$E_i(x) = \int_x^\infty \frac{\exp(-u)}{u}\,du. \tag{45}$$

Equation (44) can be recast into

$$T(\rho,t) = \frac{Q_0}{4\pi\kappa} E_i\left(\frac{\rho^2}{4\,D\,t}\right), \tag{46}$$

with E_i being a decreasing function, the temperature anywhere in the layer diverges over time at any location ρ. This result is consistent with the results that no steady state temperature profile exists when heating a 2D system (see Sec. III D).

IV. THERMOPLASMONICS OF NANOHOLES

The system now consists of a multilayer, as in the previous part, where the middle, metal layer is pierced by a cylindrical nanohole. For a plain metal layer, we have seen that a surface plasmon resonance (SPR) can be excited only with a large angle of incidence (Fig. 2) and only with an illumination from the glass side (not from the water side). These restrictions stems from mismatch of vector components of light and surface plasmons at the interfaces. However, when a defect is present, that is, any breakage of the translational symmetry, then propagating plasmons (SPP) can be excited by the wave vector components of the defect's near-field, even at normal incidence. Such defects can be nanoholes or even particles deposited on the metal layer. Moreover, a localized plasmon resonance (LPR) can also occur at the defect location, in our case the nanohole. The plasmonic resonance of a nanohole is supposed to match the one of the inverse geometry following the Babinet's principle.[16,76–79] These features make a nanohole system much richer and valuable for the numerous applications cited in the Introduction, compared with nanoparticles. However, it also makes the system more complex. Figure 7 shows a scanning electron microscope (SEM) image of a nanohole in a Au/Cr/glass layer system, fabricated by focused ion-beam lithography. For this kind of system, a relevant question is how much light is absorbed compared with a uniform metal layer as treated in the previous part. There is less absorbing material, but the possible excitation of localized and propagating plasmons may increase the absorption. So less material does not necessarily mean here less absorption, *a priori*. In this section, we investigate this question in detail.

A. Definition of the absorption cross section of nanohole

The optical absorption properties of a *nanoparticle* are characterized by its absorption cross section, defined as

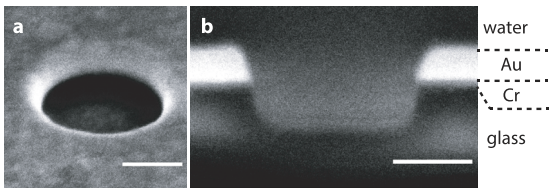

FIG. 7. Scanning electron microscope images of an experimental 300 nm diameter nanohole etched using focus ion beam on a 100 nm thick gold layer. (a) Tilted view and (b) cross section. The chromium adhesion layer is clearly visible as a thin gray layer between the gold layer (white) and the glass substrate (black). Scale bars: 150 nm. Courtesy of Jean-Benoit Claude and Jerome Wenger.

$$\sigma_{\text{abs}} = \frac{P_{\text{abs}}}{I_0}, \tag{47}$$

where P_{abs} is the absorbed power and I_0 is the irradiance of the light (power per unit area).

A nanohole is also responsible for a local variation of light absorption, but the definition of an absorption cross section is not as straightforward for a nanohole. In particular, the total power absorbed by the pierced layer does not only depend on the irradiance I_0 of the incoming light, like with a nanoparticle. It also depends on the beam size and diverges for infinite beam size due to the absorption of the metal layer itself. Thus, we propose in this Tutorial a definition of the absorption cross section of a nanohole σ_{abs} that mimics the one of a nanoparticle,

$$\sigma_{\text{abs}} = \frac{1}{I_0}\lim_{R\to\infty}\int_0^R\int_0^{2\pi}\int_0^h \left(q(\mathbf{r}) - q_{\text{layer}}(z)\right) r dz d\theta dr, \tag{48}$$

where q_{layer} is the heat power density of the plain layer [defined by Eq. (11)], without nanohole, and I_0 is the irradiance. Defined this way, this absorption cross section possesses all the properties of a conventional cross section: it has the dimension of a surface, it equals zero when the nanohole disappears, it is not dependent of the beam size for sufficiently large beam size, it does not diverge for infinitely large beam size, and, more importantly, it can be used to write

$$\delta P_{\text{abs}} = \sigma_{\text{abs}} I_0, \tag{49}$$

where δP_{abs} is the absorbed power variation due to the presence of the nanohole. The only difference with nanoparticles is that σ_{abs} and δP_{abs} can be positive or negative depending on whether the nanohole contributes to enhance and reduce light absorption.

The absorption cross section we define here is not to be considered as a conventional absorption cross section, in the sense it does not result from the simple integral of the energy density being absorbed within a finite volume, and it is not related to the flux of the Poynting vector at the surface that encloses that finite volume. Nevertheless, we call this physical quantity an absorption cross section as it features all its properties. Note this definition can apply to other systems, such as a nanoparticle deposited on a metal layer, a nanoparticle at the proximity of another one, or any nano-object placed within a medium that already absorbs light in some places. Thus, Eq. (48) can be more simply and generally recast into

$$\sigma_{\text{abs}} = \frac{P_{\text{with}} - P_{\text{without}}}{I_0}, \tag{50}$$

where P_{with} and P_{without} are the absorbed powers with and without the nano-object of interest. In the case of a nanoparticle in a uniform, non-absorbing medium, $P_{\text{without}} = 0$, and one retrieves the usual expression (47). So the absorption cross section we define here can be viewed as an extension of the usual definition of an absorption cross section in the case the surrounding medium is already absorbing light at some places.

In order to compare the absorption cross sections of nanoholes of different diameters, we also define the normalized absorption cross section C_{abs} of the nanohole as the ratio between its absorption cross section σ_{abs} and its geometrical surface,

$$C_{\text{abs}} = \frac{\sigma_{\text{abs}}}{\pi a^2}. \tag{51}$$

For the sake of simplicity, we discuss only in this Tutorial the case of cylindrical nanoholes, but these newly defined quantities σ_{abs} and C_{abs} can be applied to any nanohole shape and dimension or even to any localized defect on a metal layer.

B. Numerical calculation of the absorption cross section

Unlike with nanoparticles, no closed-form expression exists for the expression of the absorption cross sections of nanoholes, which have to be calculated numerically.

σ_{abs}, as defined by Eq. (48), consists of a difference between two terms, the first one related to the pierced layer and the second one related to the plain layer. Importantly, these two terms should not be considered as absorption cross sections, which could be calculated separately because each of these terms is infinite. This is due to the fact that an infinite metal layer illuminated by a plane wave absorbs an infinite power, hence the consideration of a limit and a subtraction of the plain layer system to avoid a divergence and get a finite quantity.

Numerically calculating σ_{abs} using its definition (48) implies the volume integration over a *finite* integration radius R. Let us name $\overline{\sigma}_{abs}(R)$ the estimation of σ_{abs} for a finite radius of integration R so that

$$\sigma_{abs} = \lim_{R\to\infty} \overline{\sigma}_{abs}(R). \tag{52}$$

In the following, σ_{abs} will be approximated by $\overline{\sigma}_{abs}(R)$, and the natural question we wish to address first is what the value of R should be to ensure proper estimation. The answer depends on the wavelength or, more precisely, on the propagation length ℓ_{SPP} of the surface plasmon propagating in the metal layer [see Eq. (20)]. As displayed in Fig. 2(c), surface plasmons on gold can propagate over several tens of micrometers in the infrared range. In this case, some electromagnetic energy can travel and dissipate much further than the light beam location. Consequently, the integration radius R has to be at least on the order of the SPP propagation length to capture a proper estimation of the total absorbed energy. This effect is illustrated in Fig. 8, which plots the estimated absorption cross section $\overline{\sigma}_{abs}(R)$ as a function of the integration radius R, in the particular case of a 200 nm diameter nanohole on a 50 nm thick gold layer deposited directly (no adhesion layer) on glass and excited from the glass side. At $\lambda_0 = 450$ nm [Fig. 8(a)], the convergence is reached for small values of R in a couple of micrometers. In this case, no long range SPP is launched [since $\ell_{SPP} < \lambda_{SPP}$, see Eqs. (18) and (20)] and the absorption created by the nanoaperture is dominant. At 650 nm [Fig. 8(b)], the propagation of a SPP is having an effect on the spreading of heat generation within the metal. The calculated absorption cross section increases with R following an exponential form until it converges. R has to be at least on the order of 10 μm. For illumination in the IR range [Fig. 8(c)], the SPP propagation length can be a few tens of μm. This feature implies a much larger system to be meshed, which can make the estimation of σ_{abs} RAM-consuming.

C. Origin and characteristics of heat dissipation with nanoholes

The results of the previous part, displayed in Fig. 8, dedicated to discuss the proper choice of the integration radius R for the estimation of σ_{abs}, are also the occasion to depict the physics of energy

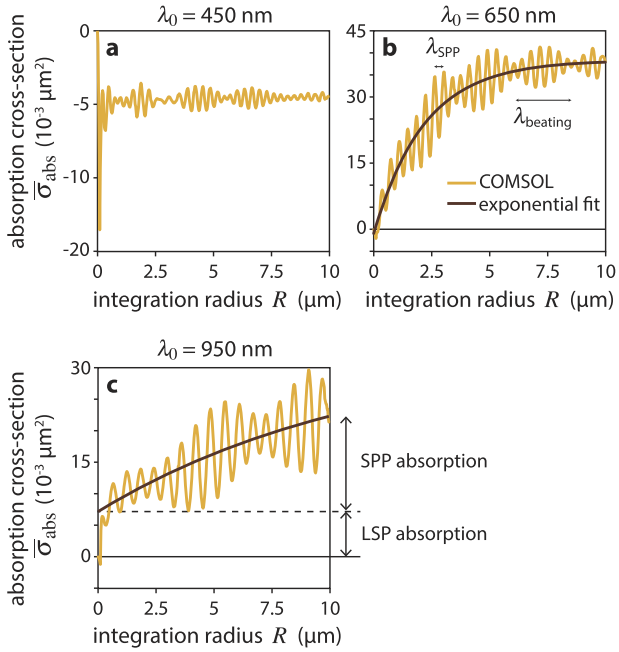

FIG. 8. Evolution of the absorption cross section of a 200 nm diameter nanohole on a 50 nm thick gold layer with the radius of integration for an excitation at (a) 450, (b) 650, and (c) 950 nm. At 450 nm, gold cannot support surface plasmons; therefore, the loss of material in the nanohole induces a decrease in the absorption. At 650 and 950 nm, plasmon-induced absorption enhancement induces a positive absorption cross section. The exponential increase in the absorption cross section with the distance is due to the progressive absorption of the SPP launched at the nanohole. High frequency oscillations can be attributed to interactions between SPP at the water–glass interface and either the transmitted light (λ_{SPP}) or the SPP at the glass–gold interface (λ_{beat}).

dissipation when illuminating a nanohole in a metal layer. With a nanohole pierced in a metal layer, two kinds of plasmons can be excited, a LPR, which locally exists at the vicinity of the hole, and SPPs, the excitation of which from the far field are made effective, thanks to the presence of the nanohole that breaks the invariance by translation throughout the metal layer. These two transduction pathways lead to two energy dissipation pathways. The first one is localized at the vicinity at the nanohole, while the other one, only possible in the IR range, can extend over several tens of micrometers. The relative effects of LPR and SPP can be observed in Fig. 8(c). At short R, one can notice a first offset, of the absorption, which results from the LPR dissipation, and a progressive increase in the estimated absorption as a function of R arising from the SPP spatial extension.

Aside from these global variations, two high frequency oscillations can be observed. The wavelength of the higher frequency one is equal to the SPP wavelength at the glass/gold interface. It can be attributed to an interference phenomenon between the incident light field and the propagative surface plasmons on the water side. The lower frequency beating ω_{beat} is assigned to the frequency difference between the SPPs at the water–gold ($\omega_{SPP-water}$) and glass–gold ($\omega_{SPP-glass}$) interfaces, following the relation $\omega_{beat} = \omega_{SPP-glass} - \omega_{SPP-water}$ (see Sec. 4 of the supplementary material for a detailed calculation).

The other interesting feature illustrated by Fig. 8(a) is the possible occurrence of negative values of the absorption cross section for nanoholes, a feature that has no counterpart in the case of nanoparticles. The possibility to have negative values of σ_{abs} for nanoholes arises from its definition as a difference between two terms, the absorption of the pierced layer and the absorption of the plain layer. Negative values of σ_{abs} mean that the presence of the nanohole reduces light absorption. As discussed further on, this effect only occurs at short wavelengths (below 500 nm) or, of course, above a certain nanohole size, when too much material is removed.

D. Effect of nanohole diameter and the layer thickness

In order to discuss the geometrical parameters of a nanohole affecting the light absorption, we computed the absorption cross section for four hole diameters and two layer thicknesses (Fig. 9).

Even if slight differences can be observed between the case of the 50 nm [Figs. 9(a) and 9(c)] and the 100 nm [Figs. 9(b) and 9(d)] thick layers, the overall shapes of the curves are similar, meaning that the layer thickness only has a marginal effect on the absorption of the nanohole.

The effect of the nanohole diameter is, however, much more pronounced, with an absorption maximum matching the plasmonic resonance frequency of the nanohole. The normalized absorption cross section [Figs. 9(c) and 9(d)] reaches values that can be higher than 1, meaning that the power absorbed by a pierced layer and converted into heat is higher than the power of the light geometrically reaching the nanohole. This behavior is similar to what can be observed with plasmonic nanoparticles[80,81] and predicted by Mie theory.[82]

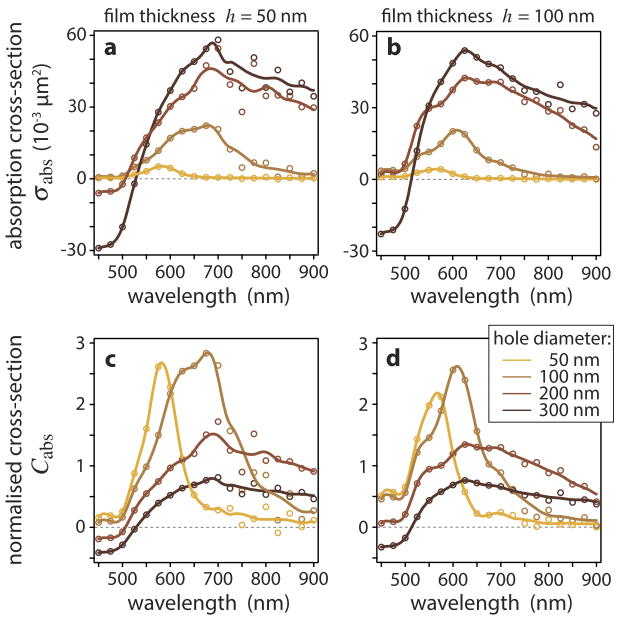

FIG. 9. (a) Absorption cross sections of nanoholes with diameters ranging from 50 to 300 nm in a 50-nm thick gold layer. (b) Same as (a) for a 100-nm thick gold layer. (c) and (d) Same as (a) and (b) where the cross sections have been normalized by the area of the nanohole.

Below 550 nm, however, the absorption cross section is low and can even become negative. As already discussed, this is because in this wavelength range, gold behaves as a simple absorber, characterized by a strong increase in the imaginary part of the permittivity due to interband transitions. This feature cancels any plasmonic effect, and the dominant rule becomes simple: less material, less absorption. This rule of thumb originates from the balance between two scaling laws: First, an absorption decrease related to the removal of material scaling as $-\pi a^2$ (the surface of the nanohole); second, an absorption increase arising from the edge of the nanohole scaling as $2\pi a$. Thus, for sufficiently large nanohole radius a, the first contribution dominates, making σ_{abs} negative.

Figures 10(a)–10(c) plots results of Comsol simulations of the temperature and heat power density associated with a 100-nm nanohole in a 100-nm thick gold film, illuminated with a focused laser at $\lambda_0 = 650$ nm and a power of 1 mW. This wavelength corresponds to the LPR resonance. The temperature map is similar to the one of a plain layer (see Fig. 4). However, the heat power density looks localized at the boundary of the nanohole. These simulations were obtained using the `Temperature_nanohole.mph` Comsol program provided in the supplementary material.

E. Effect of the wavelength

We now consider a gold layer deposited on glass with a chromium adhesion layer. As discussed in Sec. II G, light absorption can be markedly enhanced by the presence of an adhesion layer, leading the community to usually illuminate the sample from the water side for trapping applications, for instance.[64] In the following, both illumination directions will be considered from the water and the glass sides [Fig. 11(a)]. In this section, we consider only a hole diameter of 200 nm. The COMSOL program provided in the supplementary material can be used to compute any other configuration.

Figures 11(b) and 11(c) compare the effect of the wavelength. At 450 nm, gold behaves as a simple absorber, like chromium [Figs. 3(h) and 3(i)]. No surface plasmon can be excited. In any case, the absorption cross section is slightly negative when using an excitation wavelength below 500 nm, in agreement with Fig. 9. The amount of light absorbed, with or without nanohole, is mainly dictated by the size of the metal surface under illumination. Without nanohole, this surface just corresponds to the beam profile. The presence of a nanohole removes a surface πR_{laser}^2 of the layer, decreasing the absorption, but adds another area $2\pi R_{laser} h$, that is, the inner wall surface of the hole, which increases absorption accordingly. The balance of these two contributions can be considered to explain the behavior observed in Figs. 11(b) and 11(c). The reason why σ_{abs} remains very small (compared with the 700 nm case discussed later on) is that the two surface πR_{laser}^2 and $2\pi R_{laser} h$ are almost equal: the removed surface of the layer is replaced by the nanohole inner walls. The addition of the chromium layer increases the absorption (makes it less negative), no matter the illumination side, mainly because it increases the layer thickness and thus the total amount of the metal. Shining from the water side also increases the absorption of the nanohole. This effect comes from

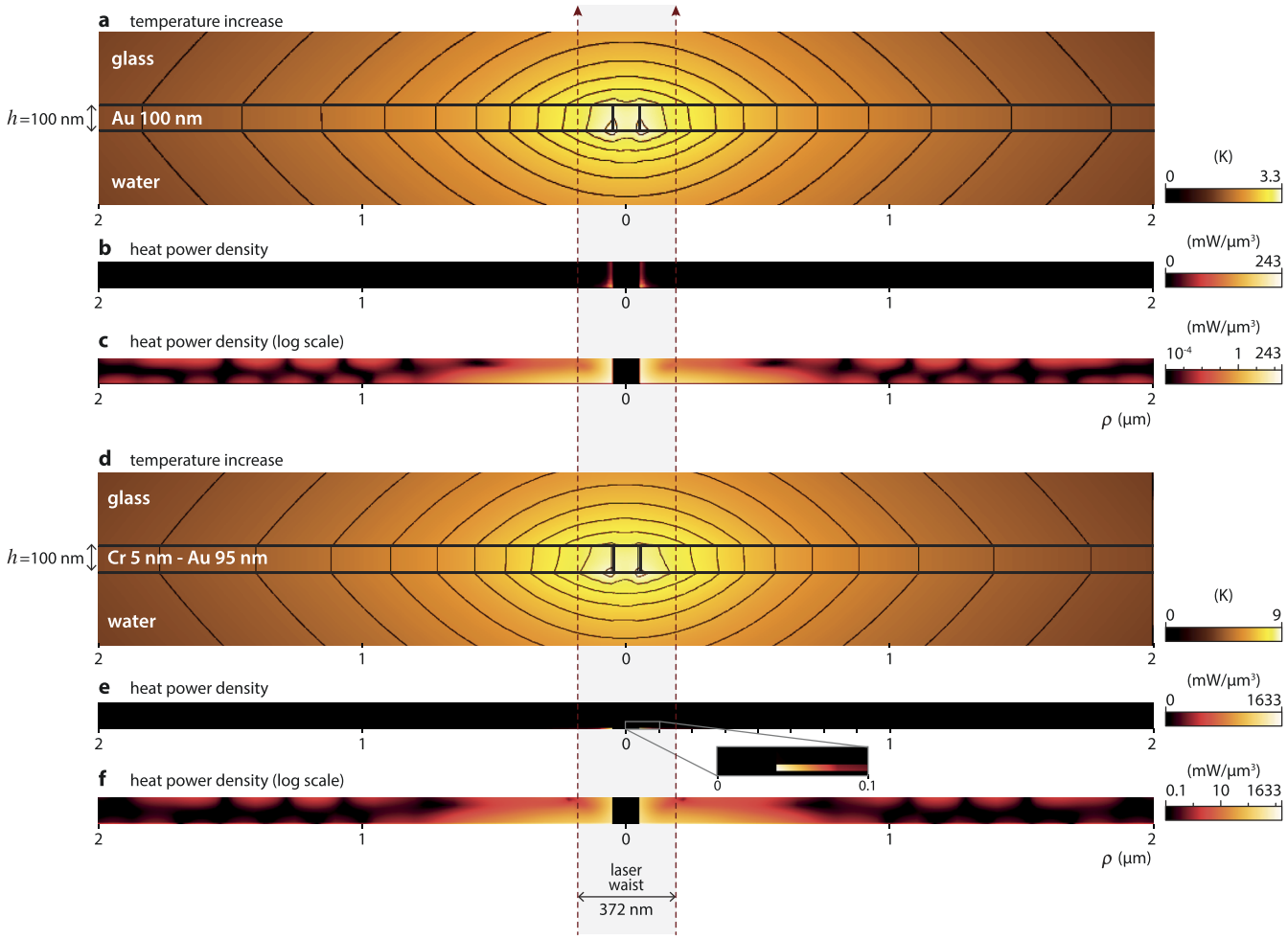

FIG. 10. Comsol simulations of the heat power density and the temperature distributions in a glass/metal/water system pierced with a nanohole and illuminated by a focused laser beam at $\lambda_0 = 650$ nm. (a) Temperature distribution for a gold layer, 100-nm thick and 100-nm nanohole. (b) Associated heat power density. (c) Same as (b) in log colorscale. (d)–(f) Same as (a)–(c) for a 95-nm thick gold layer adhering on a 5-nm thick Cr layer. In (e), a zoom window highlights the heat generation confined in the thin Cr adhesion layer.

the absorbance A of a continuous gold layer that is about 15% larger when excited from the glass side (see Fig. 3), increasing q_{layer} of Eq. (48).

Let us now discuss the more complicated case of the excitation in the red–infrared region, where absorption is also affected by plasmonic effects. At 700 nm [Fig. 11(c)], all the absorption cross sections are positive, meaning that the presence of the hole increases the amount of absorbed energy compared with a plain layer. Let us start with the comparison of a gold layer without the adhesion layer (cases 1 vs 3). The absorbances of a plain Au layer excited either from the glass or from the water side are similar [see Eq. (9) for the calculation]: 3.62% from the water side and 4.05% from the glass side, i.e., 10% variation. Therefore, the strong difference in absorption cross section observed in Fig. 11(c) (case 1 vs case 3) is not due to variations of plain layer absorbance. The difference comes from a more efficient excitation of surface plasmons from the glass side due to a better match of the wave vectors: $k_{\text{SPP}} > k_{\text{glass}} > k_{\text{water}}$.

F. Effect of the adhesion layer

Let us now focus on the effect of the adhesion layer and start with the glass side illumination, still at 700 nm [Fig. 11(c), cases 1 vs 2]. Counter-intuitively, the presence of a Cr layer strongly reduces the absorption cross section. This counterintuitive effect comes from the definition of the absorption cross section, given by Eq. (48): the subtracted term q_{layer} is larger in the presence of chromium, leading to a reduced calculated absorption cross section. One has to keep in mind that the absorption cross section as defined in this Tutorial is a comparison with a plain layer, considered as a reference. Thus, two absorption cross sections cannot be really compared with each other if they correspond to different layer geometry. In particular, they cannot be compared to predict relative temperature increases, as illustrated by Fig. 11(f). At the same wavelength of 700 nm, while a hole in a gold layer (case 1) has a larger absorption cross section than with a Cr adhesion layer, it, however, yields

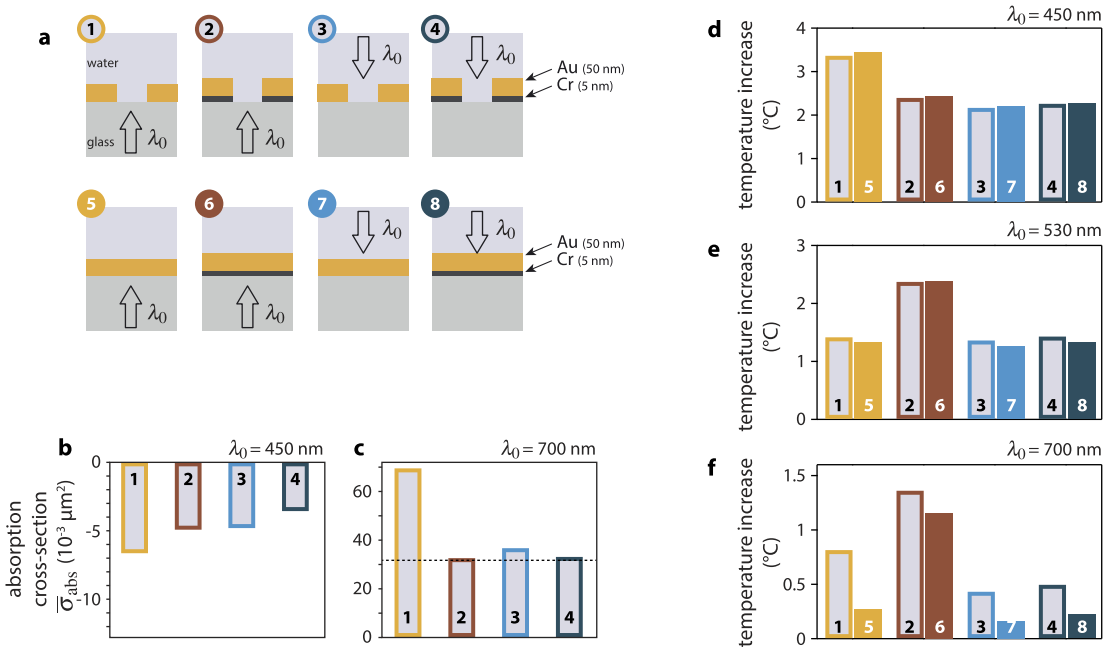

FIG. 11. (a) Geometries considered by the COMSOL calculations of absorption cross sections and temperature increases of nanohole systems. The nanoholes are 200 nm in diameter, the Ay layer is 50 nm thick, and the Cr layer is 5 nm thick. (b) Absorption cross sections of nanoholes calculated at λ_0 = 450 nm. (c) Same as (b) for λ_0 = 700 nm. The dotted line represents the area of the hole. (d) Calculation of the temperature increase for the eight geometries depicted in (a) and for λ_0 = 450 nm, for an incident power of 1 mW, and a Gaussian spot with a full-width half-maximum of $\lambda_0/2n$. (e) Same as (d) for λ_0 = 530 nm. (f) Same as (d) for λ_0 = 700 nm.

a weaker temperature increase. An example of temperature and heat power density distribution is given in Figs. 10(d)–10(f).

To end this section, we wish to notice that all the descriptions and the theory described so far could be applied to nanostructures on top of metal film, not only for nanoholes. Nanostructures would also have LPR that could couple to SPP, for which absorption cross section could also be defined by Eq. (48). Addressing such a system is out of the scope of this Tutorial. However, it could straightforwardly be modeled by adapting the Comsol program `Temperature_nanohole.mph` provided in the supplementary material.

V. CONCLUSION

This Tutorial intends to provide a comprehensive description of the photothermal effects that can occur when illuminating a metal layer, without and with the presence of nanohole. The aim is to tackle all the aspects of the problem, from the physics, to the numerical approaches. We investigate and discuss the influence of parameters such as the layer composition, thickness, the presence of an adhesion layer, the illumination wavelength, incidence angle, polarization, and the nanohole size. We also define the absorption cross section of a nanohole and discuss its meaning in the case of a 50-nm thick gold layer, with or without chromium adhesion layer.

We also provide in the supplementary material all the numerical codes used in this Tutorial, namely, (i) the Matlab code for Fresnel coefficients calculations, (ii) the Mathematica code for the calculation of Green's function for a three-layer system, (iii) the Matlab code for Green's function calculation of the temperature profile in a metal layer, (iv) the Comsol program for the calculation of the temperature profile in a metal layer under focused illumination, and (v) the Comsol program for the calculation of the temperature profile in a metal layer pierced with a nanohole.

Thermoplasmonics led to numerous applications based on desired photothermal effects of plasmonic nanoparticles. However, photothermal effects may also be unexpected and unwanted. In the latter case, careful attention to the temperature increase has to be paid to avoid sample damage or misleading interpretation of the results, like recently evidenced in plasmonic-assisted nanochemistry[83] or optical trapping.[47,64] Considering the increasing amount of studies involving metal films in plasmonics and nanoapertures (and no longer nanoparticles), photothermal effects will also have to be carefully considered in layer geometries, albeit much more complex.

SUPPLEMENTARY MATERIAL

See the supplementary material for access to all the Matlab, 1093 Comsol, and Mathematica numerical codes that have been used to com pute the data presented in this Tutorial.

ACKNOWLEDGMENTS

This work was supported by the Agence Nationale de la Recherche (SeqSynchro, Grant No. ANR-18-CE42-0013).

AUTHOR DECLARATIONS

Conflict of Interest

The authors have no conflicts to disclose.

DATA AVAILABILITY

The data that support the findings of this study are available within the article and its supplementary material.

REFERENCES

[1] S. A. Maier, *Plasmonics, Fundamentals and Applications* (Springer, 2007).
[2] M. Pelton, J. Aizpurua, and G. Bryant, "Metal-nanoparticle plasmonics," Laser Photonics Rev. **2**, 136–159 (2008).
[3] E. Boisselier and D. Astruc, "Gold nanoparticles in nanomedicine: Preparations, imaging, diagnostics, therapies and toxicity," Chem. Soc. Rev. **38**, 1759–1782 (2009).
[4] J. Langer, D. Jimenez de Aberasturi, J. Aizpurua, R. A. Alvarez-Puebla, B. Auguié, J. J. Baumberg, G. C. Bazan, S. E. J. Bell, A. Boisen, A. G. Brolo, J. Choo, D. Cialla-May, V. Deckert, L. Fabris, K. Faulds, F. J. García de Abajo, R. Goodacre, D. Graham, A. J. Haes, C. L. Haynes, C. Huck, T. Itoh, M. Käll, J. Kneipp, N. A. Kotov, H. Kuang, E. C. Le Ru, H. K. Lee, J.-F. Li, X. Y. Ling, S. A. Maier, T. Mayerhöfer, M. Moskovits, K. Murakoshi, J.-M. Nam, S. Nie, Y. Ozaki, I. Pastoriza-Santos, J. Perez-Juste, J. Popp, A. Pucci, S. Reich, B. Ren, G. C. Schatz, T. Shegai, S. Schlücker, L.-L. Tay, K. G. Thomas, Z.-Q. Tian, R. P. Van Duyne, T. Vo-Dinh, Y. Wang, K. A. Willets, C. Xu, H. Xu, Y. Xu, Y. S. Yamamoto, B. Zhao, and L. M. Liz-Marzán, "Present and future of surface-enhanced Raman scattering," ACS Nano **14**, 28–117 (2020).
[5] K. A. Willets and R. P. Van Duyne, "Localized surface plasmon resonance spectroscopy and sensing," Annu. Rev. Phys. Chem. **58**, 267–297 (2007).
[6] S.-H. Oh and H. Altug, "Performance metrics and enabling technologies for nanoplasmonic biosensors," Nat. Commun. **9**, 5263 (2018).
[7] G. Baffou and R. Quidant, "Nanoplasmonics for chemistry," Chem. Soc. Rev. **43**, 3898–3907 (2014).
[8] U. Aslam, V. G. Rao, S. Chavez, and S. Linic, "Catalytic conversion of solar to chemical energy on plasmonic metal nanostructures," Nat. Catal. **1**, 656–665 (2018).
[9] M. L. Brongersma, N. J. Halas, and P. Nordlander, "Plasmon-induced hot carrier science and technology," Nat. Nanotechnol. **10**, 25–34 (2015).
[10] M. A. Green and S. Pillai, "Harnessing plasmonic for solar cells," Nat. Photonics **6**, 130–132 (2012).
[11] K. R. Catchpole and A. Polman, "Plasmonic solar cells," Opt. Express **16**, 21793 (2008).
[12] S. C. Warren and E. Thimsen, "Plasmonic solar water splitting," Energy Environ. Sci. **5**, 5133 (2012).
[13] H. H. Nguyen, J. Park, S. Kang, and M. Kim, "Surface plasmon resonance: A versatile technique for biosensor applications," Sensors **15**, 10481–10510 (2015).
[14] *Real-Time Analysis of Biomolecular Interactions*, edited by K. Nagata and H. Handa (Springer, 2000).
[15] V. G. Kravets, A. V. Kabashin, W. L. Barnes, and A. N. Grigorenko, "Plasmonic surface lattice resonances: A review of properties and applications," Chem. Rev. **118**, 5912–5951 (2018).
[16] T. Rindzevicius, Y. Alaverdyan, B. Sepulveda, T. Pakizeh, M. Käll, R. Hillenbrand, J. Aizpurua, and F. J. García de Abajo, "Nanohole plasmons in optically thin gold films," J. Phys. Chem. C **111**, 1207–1212 (2007).
[17] A. Danilov, G. Tselikov, F. Wu, V. G. Kravets, I. Ozerov, F. Bedu, A. N. Grigorenko, and A. V. Kabashin, "Ultra-narrow surface lattice resonances in plasmonic metamaterial arrays for biosensing applications," Biosens. Bioelectron. **104**, 102–112 (2018).
[18] D. Kotlarek, S. Fossati, P. Venugopalan, N. Gisbert Quilis, J. Slabý, J. Homola, M. Lequeux, F. Amiard, M. Lamy de la Chapelle, U. Jonas, and J. Dostálek, "Actuated plasmonic nanohole arrays for sensing and optical spectroscopy applications," Nanoscale **12**, 9756–9768 (2020).
[19] D. Verschueren, X. Shi, and C. Dekker, "Nano-optical tweezing of single proteins in plasmonic nanopores," Small Methods **3**, 1800465 (2019).
[20] M. L. Juan, R. Gordon, Y. Pang, F. Eftekhari, and R. Quidant, "Self-induced back-action optical trapping of dielectric nanoparticles," Nat. Phys. **5**, 915–919 (2009).
[21] Y. Pang and R. Gordon, "Dielectric spheres using double-nanoholes in a gold film," Nano Lett. **11**, 3763–3767 (2011).
[22] K. Wang, E. Schonbrun, P. Steinvurzel, and K. B. Crozier, "Trapping and rotating nanoparticles using a plasmonic nano-tweezer with an integrated heat sink," Nat. Commun. **2**, 469 (2011).
[23] J. Berthelot, S. S. Aćimović, M. L. Juan, M. P. Kreuzer, J. Renger, and R. Quidant, "Three-dimensional manipulation with scanning near-field optical nanotweezers," Nat. Nanotechnol. **9**, 295–299 (2014).
[24] A. A. E. Saleh and J. A. Dionne, "Toward efficient optical trapping of sub-10-nm particles with coaxial plasmonic apertures," Nano Lett. **12**, 5581–5586 (2012).
[25] X. Han, V. G. Truong, P. S. Thomas, and S. N. Chormaic, "Sequential trapping of single nanoparticles using a gold plasmonic nanohole array," Photonics Res. **6**, 981–986 (2018).
[26] D. Garoli, H. Yamazaki, N. Maccaferri, and M. Wanunu, "Plasmonic nanopores for single-molecule detection and manipulation: Toward sequencing applications," Nano Lett. **19**, 7553–7562 (2019).
[27] X. Shi, D. V. Verschueren, and C. Dekker, "Active delivery of single DNA molecules into a plasmonic nanopore for label-free optical sensing," Nano Lett. **18**, 8003–8010 (2018).
[28] T. W. Ebbesen, H. J. Lezec, H. F. Ghaemi, T. Thio, and P. A. Wolff, "Extraordinary optical transmission through sub-wavelength hole arrays," Nature **391**, 667–669 (1998).
[29] F. J. García de Abajo, "Light transmission through a single cylindrical hole in a metallic film," Opt. Express **10**, 1475–1484 (2002).
[30] T. Shen, Q. Tan, Z. Dai, N. P. Padture, and D. Pacifici, "Arrays of plasmonic nanostructures for absorption enhancement in perovskite thin films," Nanomaterials **10**, 1342 (2020).
[31] P. Candeloro, E. Iuele, G. Perozziello, M. L. Coluccio, F. Gentile, N. Malara, V. Mollace, and E. Di Fabrizio, "Plasmonic nanoholes as SERS devices for biosensing applications: An easy route for nanostructures fabrication on glass substrates," Microelectron. Eng. **175**, 30–33 (2017), part of Special Issue: Micro- and Nanotechnology/engineering for Life Sciences and Biology.
[32] X. Luo, Y. Xing, D. D. Galvan, E. Zheng, P. Wu, C. Cai, and Q. Yu, "Plasmonic gold nanohole array for surface-enhanced Raman scattering detection of DNA methylation," ACS Sens. **4**, 1534–1542 (2019).
[33] B. Ai, Z. Wang, H. Möhwald, and G. Zhang, "Plasmonic nanochemistry based on nanohole array," ACS Nano **11**, 12094–12102 (2017).
[34] D. Tordera, D. Zhao, A. V. Volkov, X. Crispin, and M. P. Jonsson, "Thermoplasmonic semitransparent nanohole electrodes," Nano Lett. **17**, 3145–3151 (2017).
[35] G. Baffou, C. Girard, and R. Quidant, "Mapping heat origin in plasmonics structures," Phys. Rev. Lett. **104**, 136805 (2010).
[36] O. Lozan, M. Perrin, B. Ea-Kim, J. M. Rampnoux, S. Dilhaire, and P. Lalanne, "Anomalous light absorption around subwavelength apertures in metal films," Phys. Rev. Lett. **112**, 193903 (2014).
[37] Z.-Z. J. Lim, J.-E. J. Li, C.-T. Ng, L.-Y. L. Yung, and B.-H. Bay, "Gold nanoparticles in cancer therapy," Acta Pharmacol. Sin. **32**, 983–990 (2011).
[38] J. Qiu and W. David Wei, "Surface plasmon-mediated photothermal chemistry," J. Phys. Chem. C **118**, 20735–20749 (2014).
[39] G. Baffou and R. Quidant, "Thermo-plasmonics: Using metallic nanostructures as nano-sources of heat," Laser Photonics Rev. **7**, 171–187 (2013).
[40] G. Baffou, *Thermoplasmonics: Heating Metal Nanoparticles with Light* (Cambridge University Press, 2017).
[41] G. Baffou, F. Cichos, and R. Quidant, "Applications and challenges of thermoplasmonics," Nat. Mater. **19**, 946–958 (2020).
[42] L. Jauffred, A. Samadi, H. Klingberg, P. M. Bendix, and L. B. Oddershede, "Plasmonic heating of nanostructures," Chem. Rev. **119**, 8087–8130 (2019).
[43] A. Passian, A. L. Lereu, E. T. Arakawa, R. H. Ritchie, T. Thundat, and T. L. Ferrell, "Opto-electronic versus electro-optic modulation," Appl. Phys. Lett. **85**, 2703 (2004).

[44]A. Passian, A. L. Lereu, E. T. Arakawa, A. Wig, T. Thundat, and T. L. Ferrell, "Modulation of multiple photon energies by use of surface plasmons," Opt. Lett. **30**, 41–43 (2005).
[45]A. Passian, S. Zahrai, A. L. Lereu, R. H. Farahi, T. L. Ferrell, and T. Thundat, "Nonradiative surface plasmon assisted microscale Marangoni forces," Phys. Rev. E **73**, 066311 (2006).
[46]A. A. Al Balushi and R. Gordon, "A label-free untethered approach to single-molecule protein binding kinetics," Nano Lett. **14**, 5787–5791 (2014).
[47]Q. Jiang, B. Rogez, J.-B. Claude, G. Baffou, and J. Wenger, "Temperature measurement in plasmonic nanoapertures used for optical trapping," ACS Photonics **6**, 1763–1773 (2019).
[48]Z. Xu, W. Song, and K. B. Crozier, "Direct particle tracking observation and Brownian dynamics simulations of a single nanoparticle optically trapped by a plasmonic nanoaperture," ACS Photonics **5**, 2850–2859 (2018).
[49]G. Baffou, R. Quidant, and F. J. García de Abajo, "Nanoscale control of optical heating in complex plasmonic systems," ACS Nano **4**, 709 (2010).
[50]G. Baffou, P. Berto, E. Bermúdez Ureña, R. Quidant, S. Monneret, J. Polleux, and H. Rigneault, "Photoinduced heating of nanoparticle arrays," ACS Nano **7**, 6478–6488 (2013).
[51]M. Born and E. Wolf, *Principles of Optics: Electromagnetic Theory of Propagation, Interference and Diffraction of Light* (Cambridge University Press, 1999).
[52]S. Khadir, P. Bon, D. Vignaud, E. Galopin, N. McEvoy, D. McCloskey, S. Monneret, and G. Baffou, "Optical imaging and characterization of graphene and other 2D materials using quantitative phase microscopy," ACS Photonics **4**, 3130–3139 (2017).
[53]P. B. Johnson and R. W. Christy, "Optical constants of the noble metals," Phys. Rev. B **6**, 4370–4379 (1972).
[54]H. Raether, "Surface plasmons on smooth surfaces," in *Surface Plasmons on Smooth and Rough Surfaces and on Gratings*, Springer Tracts in Modern Physics, edited by H. Raether (Springer, 1988).
[55]*Surface Plasmon Resonance Based Sensors*, edited by J. Homola (Springer, 2006).
[56]M. Kuttge, E. J. R. Vesseur, J. Verhoeven, H. J. Lezec, H. A. Atwater, and A. Polman, "Loss mechanisms of surface plasmon polaritons on gold probed by cathodoluminescence imaging spectroscopy," Appl. Phys. Lett. **93**, 113110 (2008).
[57]N. Hiramatsu, F. Kusa, K. Imasaka, I. Morichika, A. Takegami, and S. Ashihara, "Propagation length of mid-infrared surface plasmon polaritons on gold: Impact of morphology change by thermal annealing," J. Appl. Phys. **120**, 173103 (2016).
[58]A. Kolomenski, A. Kolomenskii, J. Noel, S. Peng, and H. Schuessler, "Propagation length of surface plasmons in a metal film with roughness," Appl. Opt. **48**, 5683 (2009).
[59]L. Jason-Moller, M. Murphy, and J. Bruno, "Overview of Biacore systems and their applications," in *Current Protocols in Protein Science* (Wiley, 2006), Vol. 45, pp. 19.13.1–19.13.14.
[60]H. Aouani, J. Wenger, D. Gérard, H. Rigneault, E. Devaux, T. W. Ebbesen, F. Mahdavi, T. Xu, and S. Blair, "Crucial role of the adhesion layer on the plasmonic fluorescence enhancement," ACS Nano **3**, 2043–2048 (2009).
[61]X. Xiao, Y. Gao, J. Xiang, and F. Zhou, "Laser-induced thermal effect in surface plasmon resonance," Anal. Chim. Acta **676**, 75–80 (2010).
[62]F. Colas, D. Barchiesi, S. Kessentini, T. Toury, and M. L. de la Chapelle, "Comparison of adhesion layers of gold on silicate glasses for SERS detection," J. Opt. **17**, 114010 (2015).
[63]L. Vj, N. P. Kobayashi, M. Saif Islam, W. Wu, P. Chaturvedi, N. X. Fang, S. Y. Wang, and R. Stanley Williams, "Ultrasmooth silver thin films deposited with a germanium nucleation layer," Nano Lett. **9**, 178–182 (2009).
[64]Q. Jiang, B. Rogez, J.-B. Claude, A. Moreau, J. Lumeau, G. Baffou, and J. Wenger, "Adhesion layer influence on controlling the local temperature in plasmonic gold nanoholes," Nanoscale **12**, 2524–2531 (2020).
[65]P. K. Gothe, D. Gaur, and V. G. Achanta, "MPTMS self-assembled monolayer deposition for ultra-thin gold films for plasmonics," J. Phys. Commun. **2**, 035005 (2018).
[66]T. G. Habteyes, S. Dhuey, E. Wood, D. Gargas, S. Cabrini, P. J. Schuck, A. P. Alivisatos, and S. R. Leone, "Metallic adhesion layer induced plasmon damping and molecular linker as a nondamping alternative," ACS Nano **6**, 5702–5709 (2012).
[67]V. S. Ramanan, M. Muthukumar, S. Gnanasekaran, M. J. Venkataramana Reddy, and B. Emmanuel, "Green's functions for the Laplace equation in a 3-layer medium, boundary element integrals and their application to cathodic protection," Eng. Anal. Boundary Elem. **23**, 777–786 (1999).
[68]Q. Jiang, B. Rogez, J.-B. Claude, G. Baffou, and J. Wenger, "Quantifying the role of the surfactant and the thermophoretic force in plasmonic nano-optical trapping," Nano Lett. **20**, 8811–8817 (2020).
[69]J. Cunha, T. L. Guo, A. Nana Koya, A. Toma, M. Prato, G. Della Valle, A. Alabastri, and R. Proietti Zaccaria, "Photoinduced temperature gradients in sub-wavelength plasmonic structures: The thermoplasmonics of nanocones," Adv. Opt. Mater. **8**, 2000568 (2020).
[70]S. Link and M. A. El-Sayed, "Spectral properties and relaxation dynamics of surface plasmon electronic oscillations in gold and silver nanodots and nanorods," J. Phys. Chem. B **103**, 8410 (1999).
[71]J. H. Hodak, A. Henglein, and G. V. Hartland, "Electron-phonon coupling dynamics in very small (between 2 and 8 nm diameter) Au nanoparticles," J. Chem. Phys. **112**, 5942 (2000).
[72]F. J. García de Abajo, "Nonlocal effects in the plasmons of strongly interacting nanoparticles, dimers, and waveguides," J. Phys. Chem. C **112**, 17983–17987 (2008).
[73]O. Marti, A. Ruf, M. Hipp, H. Bielefeldt, J. Colchero, and J. Mlynek, "Mechanical and thermal effects of laser irradiation on force microscope cantilevers," Ultramicroscopy **42-44**, 345–350 (1992).
[74]G. Baffou and H. Rigneault, "Femtosecond-pulsed optical heating of gold nanoparticles," Phys. Rev. B **84**, 035415 (2011).
[75]J. M. Bennett and E. J. Ashley, "Infrared reflectance and emittance of silver and gold evaporated in ultrahigh vacuum," Appl. Opt. **4**, 221 (1965).
[76]J. Prikulis, P. Hanarp, L. Olofsson, D. Sutherland, and M. Käll, "Optical spectroscopy of nanometric holes in thin gold films," Nano Lett. **4**, 1003–1007 (2004).
[77]M. Horák, V. Křápek, M. Hrtoň, A. Konečná, F. Ligmajer, M. Stöger-Pollach, T. Šamořil, A. Paták, Z. Édes, O. Metelka, J. Babocký, and T. Šikola, "Limits of Babinet's principle for solid and hollow plasmonic antennas," Sci. Rep. **9**, 4004 (2019).
[78]M. Hentschel, T. Weiss, S. Bagheri, and H. Giessen, "Babinet to the half: Coupling of solid and inverse plasmonic structures," Nano Lett. **13**, 4428–4433 (2013).
[79]T. Zentgraf, T. P. Meyrath, A. Seidel, S. Kaiser, H. Giessen, C. Rockstuhl, and F. Lederer, "Babinet's principle for optical frequency metamaterials and nanoantennas," Phys. Rev. B **76**, 033407 (2007).
[80]R. Yu, L. M. Liz-Marzán, and F. J. García de Abajo, "Universal analytical modeling of plasmonic nanoparticles," Chem. Soc. Rev. **46**, 6710–6724 (2017).
[81]J. Olson, S. Dominguez-Medina, A. Hoggard, L.-Y. Wang, W.-S. Chang, and S. Link, "Optical characterization of single plasmonic nanoparticles," Chem. Soc. Rev. **44**, 40–57 (2015).
[82]G. N. Plass, "Mie scattering and absorption cross sections for absorbing particles," Appl. Opt. **5**, 279–285 (1966).
[83]G. Baffou, I. Bordacchini, A. Baldi, and R. Quidant, "Simple experimental procedures to distinguish photothermal from hot-carrier processes in plasmonics," Light: Sci. Appl. **9**, 108 (2020).